공학박사 학위논문

Dehydro-aromatization of Natural Gas over Mo-based Catalysts

몰리브데넘 기반 촉매를 이용한 천연 가스 탈수소방향족화 반응

2023년 2월

서울대학교 대학원

화학생물공학부

류 혜 원

Dehydro-aromatization of Natural Gas over Mo-based Catalysts

지도 교수 김 도 희

이 논문을 공학박사 학위논문으로 제출함
2023년 1월

서울대학교 대학원
화학생물공학부
류 혜 원

류혜원의 공학박사 학위논문을 인준함
2023년 1월

위 원 장 _____ 이 원 보 _____ (인)

부위원장 _____ 김 도 희 _____ (인)

위 원 _____ 강 종 헌 _____ (인)

위 원 _____ 김 지 만 _____ (인)

위 원 _____ 박 영 권 _____ (인)

Abstract

Benzene, toluene, and xylene (BTX) are crucial building blocks for the production of valuable chemicals and plastics. BTX is mainly produced as a byproduct of naphtha cracking in the production of light olefins. As the price of crude oil is highly volatile, finding an alternative fuel is mandatory. Natural gas, which is mainly composed of methane, is a promising alternative resource owing to its abundance and environmental friendliness. Non-oxidative dehydro-aromatization of methane is an effective reaction that directly converts methane to benzene, toluene, xylene (BTX), and hydrogen in a non-oxidative atmosphere. Its selectivity to benzene is between 60–80%, which makes this process attractive for benzene production. Therefore, catalytic development to enhance the performance of dehydro-aromatization was studied.

In the first study, the efficiency of NiO particles with various sizes (4, 22, 36, 45, and 101 nm) as promoters for Mo/ZSM-5 was evaluated for methane dehydro-aromatization. It was found that NiO(36nm) has the optimum size for enhancing the activity of Mo/HZSM-5. The results of temperature-programmed reduction of methane, X-ray diffraction, transmission electron microscopy, and CO chemisorption revealed that among the samples analyzed, NiO(36nm)-Mo/HZSM-5 had the highest dispersion of MoCx active sites because it had the lowest reduction temperature for NiO and

MoOx. When the NiO particle size was smaller than 22 nm, the formation of inactive $NiMoO_4$ was preferred, which caused the severe agglomeration and low dispersion of MoCx.

Next, in order to suppress coke, CO_2 could be added as a soft oxidant in the feed, which is advantageous not only for preventing coke formation but also for producing additional syngas. Furthermore, catalyst could be modified to be resistant to coke by reducing the free Brønsted acid sites where coke is concentrated, or by increasing base sites where CO_2 could be adsorbed. In this respect, Mg, which is widely used to control acidic or basic properties, was incorporated in Mo/ZSM-5 in two ways: Mg-Mo/ZSM-5(co) which was prepared by co-impregnation, and Mg/Mo/ZSM-5(seq) prepared by sequential impregnation. Catalyst characterizations revealed that Mg/Mo/ZSM-5(seq) had the least number of Brønsted acid sites but had the largest number of base sites. These changes in acid and base sites enhanced catalytic yield and stability, and the enhancement was amplified as CO_2 concentration increased to 10%.

Keyword : Natural gas, CO_2, BTX, Dehydro-aromatization, Mo/HZSM-5, NiO, Mg

Student Number : 2019-32752

Table of Contents

List of Tables

List of Figures

Chapter 1. Introduction

1.1. Non oxidative dehydro-aromatization of natural gas

Benzene, toluene, and xylene (BTX) are crucial building blocks for the production of valuable chemicals and plastics. In 2018, the global demand for benzene and xylene was 91 million tons with an expected growth of 3.5 % per year [1]. BTX is mainly produced as a byproduct of naphtha cracking in the production of light olefins. As the price of crude oil is highly volatile, finding an alternative fuel is mandatory. Natural gas, which is mainly composed of methane, is a promising alternative resource owing to its abundance and environmental friendliness. The United States Energy Information Administration predicts that natural gas production will reach more than 50 trillion cubic feet by 2050. Moreover, methane is the cleanest fossil fuel because it only contains trace amounts of nitrogen and sulfur, which are the major sources of air pollution [2]. Therefore, it is advantageous to produce BTX from methane instead of crude oil from an economic and environmental perspective. Non-oxidative dehydro-aromatization of methane has been widely studied for producing aromatic hydrocarbons from natural gas [3-5]. Its selectivity to benzene is between 60–80%, which makes this process attractive for benzene production [4].

1.2. Co-feeding light hydrocarbons and carbon dioxide

There were difficulties for the commercialization of non-oxidative

dehydro-aromatization because of the low methane conversion of 14 % at 700 ℃ [5]. Also, as high reaction temperature is necessary to activate methane, the catalyst undergoes fast deactivation due to rapid coke formation. These thermodynamic limitation on benzene formation can be minimized by the addition of alkanes or alkenes to the methane feed [4]. There were attempts to overcome high activation energy of methane by co-feeding with ethane or propane [6-8]. By co-feeding methane and reactants with higher carbon number, reaction temperature decreased and conversion of methane increased.

Shale gas, which is comprised of methane, ethane, and propane, could be used for aromatization [9,10]. The advantage of shale gas aromatization is that higher yield of BTX could be obtained without the reactant separation. Recently, Jung et al. studied the technoeconomic analysis of shale gas aromatization [11]. Instead of the reactant separation by cryogenic distillation, shale gas aromatization was found to be energy efficient for converting ethane and propane to methane, yielding aromatic hydrocarbons. However, they stated that feasibility of BTX production from shale gas remained questionable due to rapid catalyst deactivation originating from coke formation. Therefore, they suggested CO_2 co-feeding shale gas aromatization not only to prevent coke formation but also to produce additional syngas [12]. When a methanol production process using syngas was integrated after the aromatization process, overall cost efficiency increased and CO_2 emission was significantly reduced.

1.3. Mo/HZSM-5

It has been suggested that Mo and ZSM-5 are among the most suitable active metals and supports, respectively, for MDA [13]. During the reaction, Mo oxide is converted into Mo carbide, which is the active phase for CH_4 activation, at temperatures above 700 °C [3,14,15]. Although discrepancies related to the activation mechanisms exist, it is widely accepted that CH_4 is initially activated on Mo carbide, yielding hydrocarbon intermediates to produce BTX owing to the shape selectivity of the ZSM-5 support [3,14,15]. However, because MDA is thermodynamically limited, the theoretical maximum yield of benzene is only 11.7 % at 700 °C [3]. In addition, aromatic hydrocarbons can be condensed into coke, which is the most thermodynamically stable product. Coke is deposited on the active sites and blocks zeolite pores, causing the rapid deactivation of the catalyst.

1.4. Objectives

In order to overcome limited conversion and rapid deactivation of the catalysts during aromatization reaction, promoters for Mo/HZSM-5 were developed. First, we prepared various sizes of NiO particles and evaluated methane dehydro-aromatization activity of physically mixed NiO-Mo/HZSM-5. Next, Mg was used as the promoter for Mo/ZSM-5 in order to enhance catalytic activity for CO_2 co-feeding shale gas aromatization.

Chapter 2. Effect of the NiO particle size on the activity of Mo/HZSM-5 catalyst physically mixed with NiO in methane dehydro-aromatization

2.1. Introduction

Previous studies have focused on increasing methane activity and preventing deactivation using various methods, including controlling the distribution and location of Mo species [16-19], varying the structure and acidity of zeolite supports [20-22], and adding a second metal that acts as a promoter of Mo/zeolite catalysts [23-27]. Reductive pretreatment prior to the reaction was proven to be efficient in enhancing the dispersion of Mo species. The pretreatment of catalysts with diluted CH_4 gas before exposure to the reaction gas led to higher Mo dispersion [17,28]. Meanwhile, the impregnation of Fe, Co, and Ni promoters prevents catalyst deactivation by inducing the formation of carbon nanotubes (CNT) [25,26]. When these metals are added to Mo/HZSM-5 catalysts in MDA, they can condensate coke precursors by producing CNT instead of detrimental coke on the active sites.

We previously reported that when commercial NiO was added to Mo/HZSM-5 using a simple physical mixing method, the catalytic activity and stability substantially improved [29]. During the pretreatment process, NiO was converted to metallic Ni, which further decreased the reduction

temperature of MoOx. The reduction of MoOx at the low temperature suppressed the agglomeration of MoCx active sites, resulting in a higher dispersion of MoCx. In addition, the physical mixing of NiO prevented catalyst deactivation by consuming the coke precursors to produce CNT.

However, the properties of metallic Ni, the active phase for the enhancement, depend on its particle size. In the case of CH_4 reforming reactions, the CH_4 turnover frequency increases when the particle size of Ni decreases [30,31] owing to the more active edge and corner sites compared to the facet sites [31]. In addition, because carbon is preferentially deposited on Ni ensembles, smaller Ni particles lead to less carbon deposition [32,33]. It was also suggested that the crystal size of Ni should be smaller than 10 nm to inhibit coke deposition [34]. By controlling the particle size of Ni, its reactivity with CH_4 and the distribution of coke are expected to change, resulting in different promotion effects on Mo/HZSM-5. When Ni is formed through the reduction of NiO, the particle size of Ni depends on the particle size of NiO [35]. Therefore, in this study, we prepared various sizes of NiO particles and evaluated the MDA activity of physically mixed NiO-Mo/HZSM-5. In addition to the optimization of the particle size, we directly observed the interaction between NiO and MoOx as a function of the particle size and investigated its effect on MDA activity.

2.2. Experimental

2.2.1. Catalyst preparation

To prepare NiO of various sizes, commercial and synthesized NiO were utilized in this study. Commercial NiO, used in our previous study [29], was purchased from Sigma-Aldrich. For the NiO synthesis, nickel carbonate was initially prepared via precipitation. Nickel hexahydrate and urea were mixed at a molar ratio of 1:4 in deionized water at room temperature. After mixing, the solution was heated to 95 °C for 1.5 h. Precipitated nickel carbonate obtained was filtered and washed and then dried at 105 °C overnight. NiO particles of various sizes were formed via the calcination of dried nickel carbonate in air in the temperature range of 400–700 °C. Before the size determination, the synthesized NiO particles were designated as NiO(X), where X is the calcination temperature, whereas commercial NiO was denoted as NiO(Com.).

Mo/HZSM-5 was prepared using a wet impregnation method. First, commercial ZSM-5 (Si/Al_2 = 23, Alfa Aesar) was calcined at 500 °C for 4 h to convert the ammonium form to the protonated form. Mo was then impregnated into HZSM-5 using an aqueous solution of $(NH_4)_6Mo_7O_{24}\cdot 4H_2O$ (Sigma Aldrich). The impregnated samples were dried at 105 °C overnight and calcined in a muffle furnace at 500 °C for 6 h. Next, NiO was added to the calcined Mo/HZSM-5 via physical mixing using a mortar. The resulting NiO and Mo contents in the catalysts were 1.06 wt.%

and 12 wt.%, respectively.

2.2.2. Catalyst characterization

To identify the crystal structures of the metal oxides, powder X-ray diffraction (XRD) was conducted using a SmartLab diffractometer (Rigaku) with Cu Kα radiation. The samples were scanned with a step size of 0.02° at a scanning speed of 1–3°/min depending on the samples. To determine the particle size of NiO, transmission electron microscopy (TEM) and energy-dispersive spectroscopy (EDS) measurements were performed using a JEM-F200 microscope equipped with a JEOL Dual SDD system, with an accelerating voltage of 200 kV. In addition, line EDS analysis was conducted using JEM-ARM200F (Cold FEG, JEOL Ltd, Japan).

The dispersion of Mo was evaluated via CO chemisorption using an ASAP 2020 analyzer (Micromeritics). Prior to the test, the passivation layer of the reduced catalysts was removed at 700 °C using pure H_2 for 1 h. Pure CO was subsequently adsorbed at 35 °C, and CO uptake was calculated from the difference between the two isotherms.

Furthermore, the temperature-programmed reduction of methane (CH_4–TPR) was performed on fresh catalysts to investigate their reducibility using mass spectroscopy (MS, Hiden Analytical). To remove water from the sample, the reactor was heated to 200 °C and maintained at this temperature for 1 h under Ar atmosphere at a flow rate of 20 mL/min. Next, the reactor

was heated to 850 °C at a heating rate of 2 °C/min in a gas mixture composed of CH_4 (9 mL/min), He (1 mL/min), and Ar (10 mL/min), which was identical to the pretreatment gas. H_2, CH_4, CO, Ar, CO_2, and C_6H_6 intensities were acquired using the m/z values of 2, 16, 28, 40, 44, and 78, respectively.

In situ XRD was conducted to observe the phase changes during the catalyst pretreatment step. SmartLab XE diffractometer (Rigaku) was operated at 200 mA and 45 kV with Cu Kα radiation. After 0.1 g of sample was loaded, it was heated from room temperature to 650 °C at a ramping rate of 10 °C/min, in a flow of CH_4 (9 mL/min) and He (11 mL/min). The XRD measurements were initiated after 20 min of holding time at temperatures 350, 450, 550, and 650 °C, and the data were collected at a step size of 0.02° and scanning speed of 2°/min.

Temperature-programmed oxidation (TPO) of the post-reaction catalysts was performed to identify the coke species. A BEL-CAT BASIC instrument (BEL Japan Inc.) equipped with an MS detector was employed to monitor oxidation behavior; m/z values of 28 and 44 were used for the detection of CO and CO_2, respectively. The post-reaction catalysts were heated from 50 °C to 900 °C at a heating rate of 5 °C/min in a flow of 5 vol.% O_2/He. Furthermore, visible–Raman analysis of the post-reaction catalysts was carried out using a laser Raman microscope (Renishaw In via Raman microscope), in which the excitation source was a 532 nm line of a Nd:YAG

laser.

2.2.3. Catalyst evaluation

Prior to the MDA reaction, 0.2 g of the catalyst was pretreated in situ in a fixed-bed quartz reactor to convert the metal oxides to active phases, such as metallic Ni and MoCx. The pretreatment gas was composed of 45 vol.% CH_4, 5 vol.% He, and 50 vol.% Ar and passed through the reactor at a total flow rate of 20 mL/min. The reactor was initially heated to 400 °C at a ramping rate of 20 °C/min, then to 700 °C at a ramping rate of 10 °C/min, and maintained at that temperature for 10 min.

After pretreatment, the MDA reaction was initiated by feeding a 90 vol.% CH_4/He gas mixture at a flow rate of 10 mL/min at atmospheric pressure. The effluent gases were analyzed at 40 min intervals using an on-line gas chromatograph (YL6500GC). Hydrocarbons were detected using a flame ionization detector, while He, H_2, and CH_4 were detected using a thermal conductivity detector. To avoid the condensation of heavy hydrocarbons, the outlet gas lines and sampling valves were heated to 230 °C. Methane conversion, selectivity, and yield of carbon-containing products were calculated based on the carbon mass balance using He as an internal standard.

2.3. Results and discussion

2.3.1. Crystallite and particle sizes of NiO

Table 2-1 lists the average crystallite and particle sizes of NiO calcined at various temperatures, which were estimated using XRD and TEM, respectively. Prior to the size calculation, it was confirmed that all particles had XRD peaks of NiO corresponding to the (1 1 1), (2 0 0), (2 2 0), (3 1 1), and (2 2 2) planes (Figure 2-1). The average crystallite size was calculated from the (2 0 0) peak using the Scherrer equation. The average size of NiO crystallites increased from 4.1 nm to 36.8 nm when the calcination temperature was increased from 400 °C to 700 °C, and the crystallite sizes of NiO(700°C) and NiO(Com.) were similar.

However, the actual sizes of the particles determined using TEM (Figure 2-2) were slightly different from those determined via XRD, except for NiO(400°C). In the case of NiO(400°C), the average particle size was 4.5 nm, which was similar to the crystallite size (4.1 nm). As the calcination temperature increased from 400 °C to 700 °C, the average particle size increased from 4.5 nm to 44.6 nm. Meanwhile, the size of NiO(Com.) was 101.3 nm, which was more than two times larger than that of NiO(700°C). The estimated size obtained from TEM was larger than that from XRD, owing to its polycrystalline structure. It was speculated that NiO(Com.) and NiO particles calcined above 500 °C are composed of NiO crystallites with a multi-directional lattice [36]. Because the actual size is a critical factor for

CH_4 activation [30,37], it is desirable to classify the NiO particles based on their actual size rather than their crystallite size. Therefore, in the next section, new notations are used based on the size estimations derived from TEM as follows: NiO(400°C) to NiO(4nm), NiO(500°C) to NiO(22nm), NiO(600°C) to NiO(36nm), NiO(700°C) to NiO(45nm), and NiO(Com.) to NiO(101nm).

Table 2-1. Average crystallite and particle size of synthesized and commercial NiO.

Sample	Average crystallite size[a] (nm)	Average particle size[b] (nm)	Notation
NiO(400°C)	4.1	4.5	NiO(4nm)
NiO(500°C)	9.7	22.3	NiO(22nm)
NiO(600°C)	28.2	35.7	NiO(36nm)
NiO(700°C)	36.8	44.6	NiO(45nm)
NiO(Com.)	38.4	101.3	NiO(101nm)

a: Based on Scherrer Equation from XRD pattern.

b: Determined by TEM analysis.

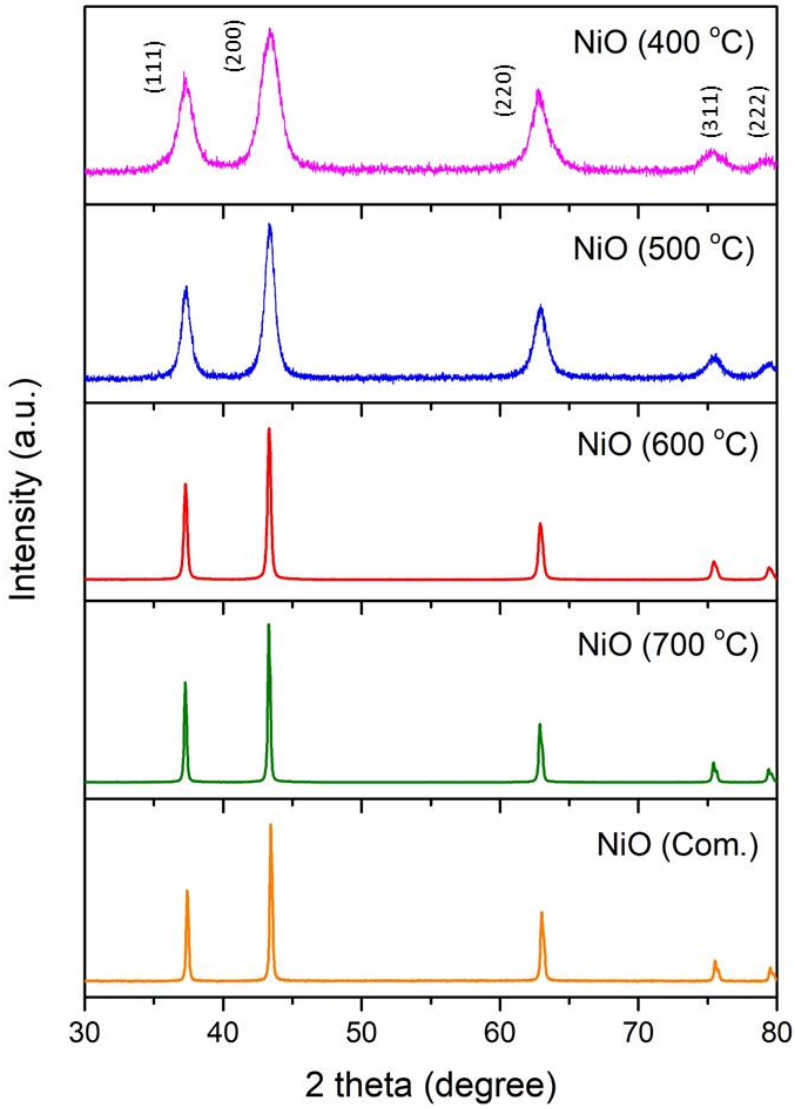

Figure 2-1. XRD patterns of synthesized and commercial NiO.

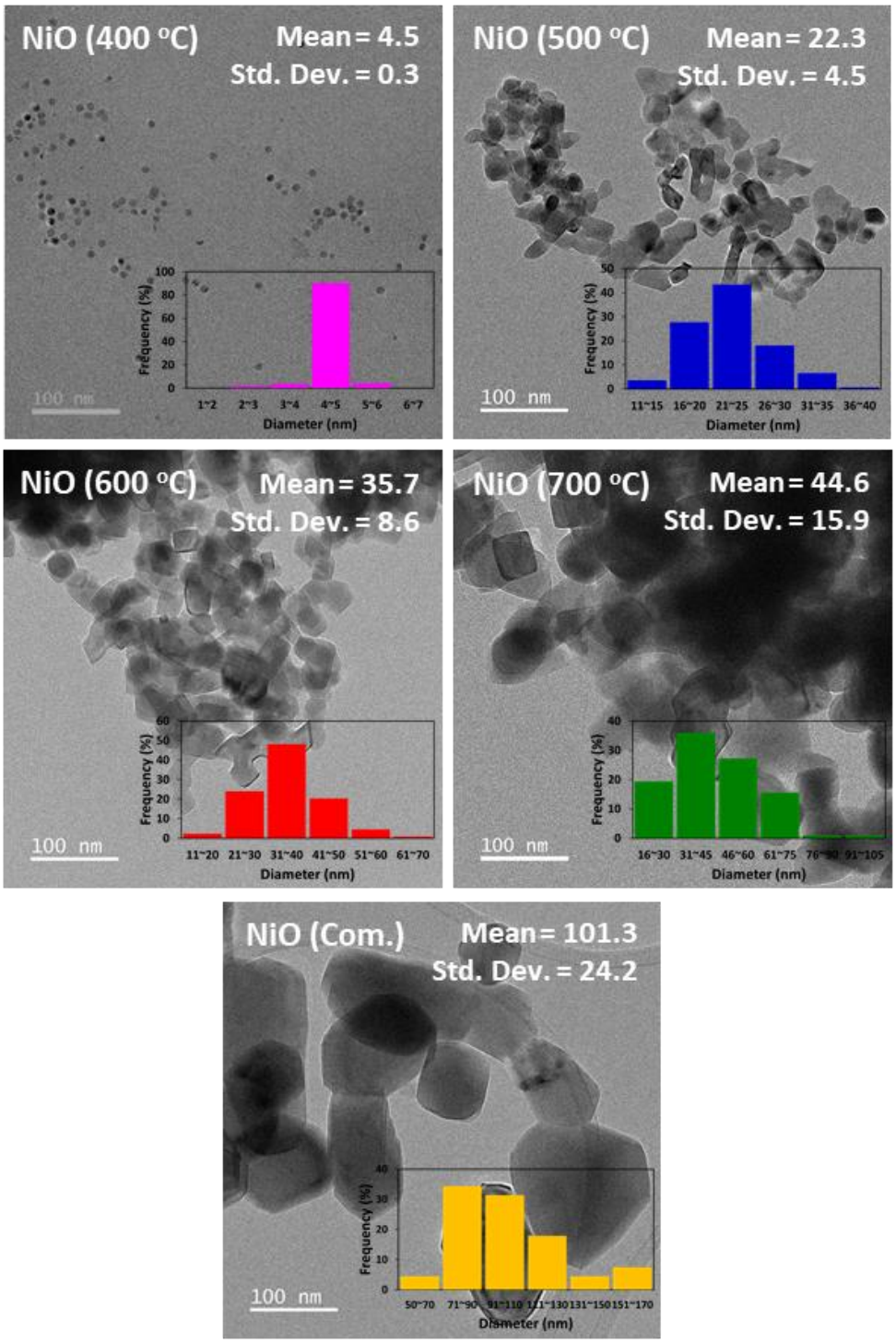

Figure 2-2. TEM images and corresponding particle size distributions of synthesized and commercial NiO.

2.3.2. MDA reactivity

The methane conversion and BTX yield of the NiO(X)-Mo/HZSM-5 catalysts, which were obtained with time-on-stream, are shown in Figure 2-3 The initial methane conversion of Mo/HZSM-5 was 9.89 %, which decreased to 3.48 % after 840 min of reaction. The highest conversion was obtained using NiO(36nm)-Mo/HZSM-5, with an initial conversion of 11.23 %, and the conversion after 840 min was 7.69 %. NiO(45nm)-Mo/HZSM-5 and NiO(101nm)-Mo/HZSM-5 had slightly lower conversions than NiO(36nm)-Mo/HZSM-5 throughout the reaction. The conversion decreased more significantly while using NiO(22nm)-Mo/HZSM-5 and NiO(4nm)-Mo/HZSM-5. In particular, for the case of NiO(4nm)-Mo/HZSM-5, the initial conversion was only 8.66 %, and the conversion after 840 min was 4.51 %.

The BTX yields of the catalysts exhibited the same tendency as the conversion. NiO(36nm)-Mo/HZSM-5 had the highest BTX yield of 6.42 % after 160 min of reaction, whereas Mo/HZSM-5 had the BTX yield of 5.10 % after 40 min of reaction. When NiO particle size was larger than 45 nm, the maximum BTX yield was limited to 6.17 %. In the case of NiO particles with sizes smaller than 22 nm, the yield decreased significantly, and NiO(4nm)-Mo/HZSM-5 had the lowest yield of 4.79 % after 40 min of reaction. Notably, the catalytic stabilities of all the NiO(X)-Mo/HZSM-5 catalysts were higher than that of Mo/HZSM-5, and NiO(36nm)-Mo/HZSM-5 was the most stable among them. After 840 min of reaction,

NiO(36nm)-Mo/HZSM-5 had the BTX yield of 5.05 %, whereas Mo/HZSM-5 had the yield of 1.51 %, indicating the superior stability of NiO(36nm)-Mo/HZSM-5 over Mo/HZSM-5.

The performance of the most active catalyst, NiO(36nm)-Mo/HZSM-5, was compared with the previous reported catalysts in Table 2-2. As catalytic performance greatly depends on various parameters such as reaction temperature, GHSV, the amount of Mo loading, Si/Al_2 ratio of zeolite and etc., we classified the literatures into three categories: literatures with the identical GHSV, or the similar Mo loading, or the same promoter, Ni. Comparing CH_4 conversion rate and BTX formation rate at 100 min and 600 min of the reaction, it was confirmed that NiO(36nm)-Mo/HZSM-5 had excellent activity and stability.

Table 2-3 lists the overall product distributions after 840 min of reaction. Mo/HZSM-5 had BTX and coke selectivities of 63.93 % and 12.94 %, respectively. When NiO(4nm) was added, BTX selectivity decreased to 61.72 %, while coke selectivity increased to 19.76 %. Furthermore, BTX selectivity increased more significantly when using the NiO-containing catalysts, compared with that obtained using Mo/HZSM-5, which resulted in a higher BTX yield, except for the case of NiO(4nm). In particular, NiO(36nm)-Mo/HZSM-5, which is the most active catalyst, had the highest BTX selectivity of 67.82 %. In addition, $C_{10}H_8$ selectivity decreased while coke selectivity increased for all the NiO-containing catalysts, and the consequences are discussed in Section 3.3.6.

To investigate the physicochemical effect of the NiO particle size on the catalytic activity of NiO(X)-Mo/HZSM-5, various characterizations were performed on the smallest, most active, and largest NiO-containing catalysts, which are NiO(4nm)-Mo/HZSM-5, NiO(36nm)-Mo/HZSM-5, and NiO(101nm)-Mo/HZSM-5, respectively.

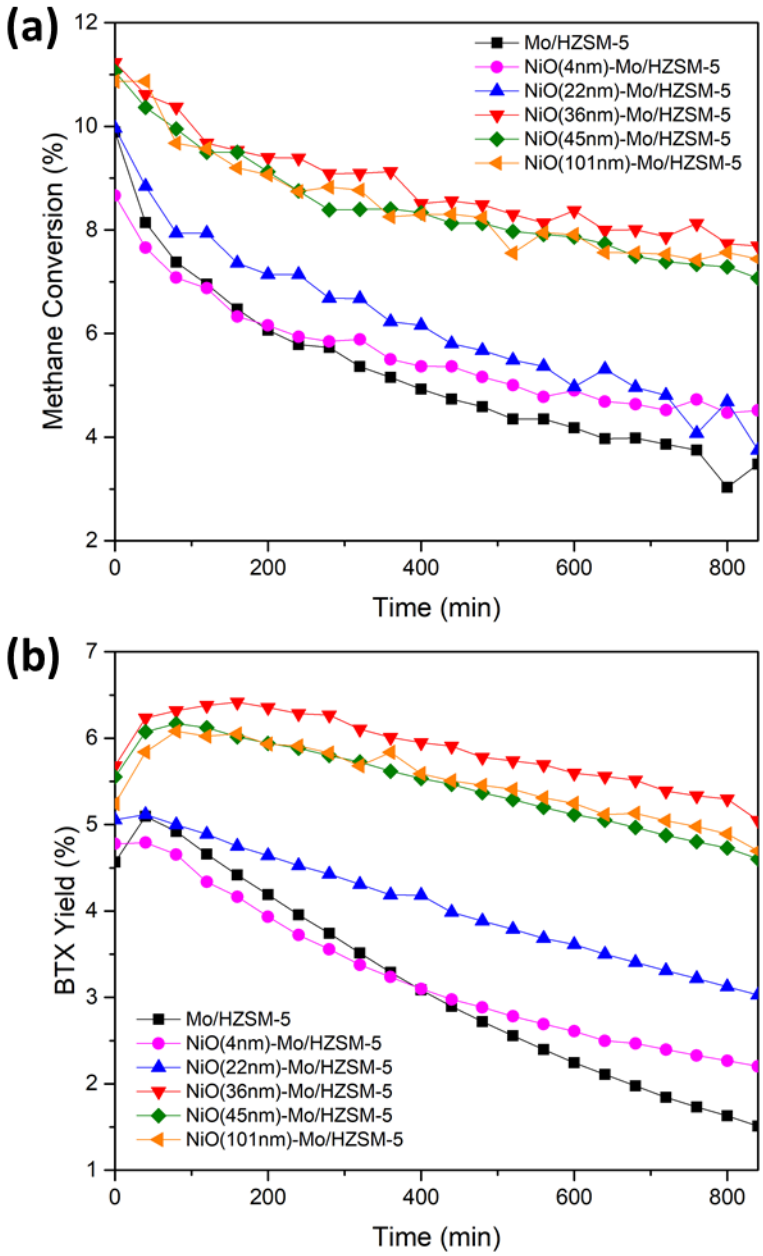

Figure 2-3. Catalytic performance of NiO(X)-Mo/HZSM-5 catalysts with various sizes of NiO: (a) Methane conversion, and (b) BTX yield.

Table 2-2. Literature review of MDA performance using Mo/zeolite-based catalysts.

Temp. (°C)	WHSV ($mL \cdot g_{cat}^{-1} \cdot hr^{-1}$)	CH_4:Ar	Mo loading (wt.%)	Promoter loading (wt.%)	Zeolite (Si/Al_2)	CH_4 conversion rate ($mmol \cdot g_{cat}^{-1} \cdot hr^{-1}$), 100 min)	BTX formation rate ($mmol \cdot g_{cat}^{-1} \cdot hr^{-1}$), 100 min)	CH_4 conversion rate ($mmol \cdot g_{cat}^{-1} \cdot hr^{-1}$), 600 min)	BTX formation rate ($mmol \cdot g_{cat}^{-1} \cdot hr^{-1}$), 600 min)	Ref.
700	3000	9:1	12	0.8 (Ni)	ZSM-5 (23)	12.54	1.27	10.13	1.13	This study
700	**3000**	9:1	4	0.3 (Fe)	ZSM-5 (55)	6.15	1.00	5.67	0.86	[38]
700	**3000**	8.5:1.5	4	-	ZSM-5 (23)	9.22	0.99	3.42	0.32	[39]
680	**3000**	9:1	5	-	MCM-22 (21)	7.47	0.60 [a]	4.34	0.36 [a]	[40]
700	1500	9:1	**10**	-	ZSM-5 (50)	8.14	1.15	7.11	0.88	[18]
700	1500	9:1	**10**	-	ZSM-5 (50)	7.96	1.00	6.09	0.84	[17]
700	1550	9.1:0.9	**10**	-	ZSM-5 (30)	7.98	0.80 [a]	7.01	0.84 [a]	[28]
700	1500	9.1:0.9	6	0.2 (**Ni**)	ZSM-5 (30)	7.01	0.70	6.34	0.65	[25]
700	1500	10:0 [b]	3	3 (**Ni**)	ZSM-5 (50)	2.01	0.22 [a]	1.67 [c]	0.18 [a,c]	[41]

a: Benzene yield
b: Feed - Natural gas (96.2 % methane, 2.3 % ethane, and the remaining is C3–C5 amounting to 1.5 %)
c: Data point at 240 min of reaction.

Table 2-3. Overall product distributions (%) of NiO(X)-Mo/HZSM-5 catalysts with various sizes of NiO.

Catalyst	C2	C3	BTX	$C_{10}H_8$	Coke
Mo/HZSM-5	10.54	0.56	63.93	12.02	12.94
NiO(4nm)-Mo/HZSM-5	8.39	0.35	61.72	9.78	19.76
NiO(22nm)-Mo/HZSM-5	9.68	0.30	65.38	8.99	15.65
NiO(36nm)-Mo/HZSM-5	5.67	0.22	67.82	8.58	17.71
NiO(45nm)-Mo/HZSM-5	6.25	0.25	65.78	6.82	20.90
NiO(101nm)-Mo/HZSM-5	5.96	0.23	66.34	7.24	20.23

2.3.3. Changes in the particle size and dispersion during the reaction

The phase transition and crystallite size of Ni and Mo species were investigated using XRD on samples collected after the pretreatment (Figure 2-4(a)) and after 840 min of reaction (Figure 2-4(b)). The NiO(36nm)- and NiO(101nm)-containing catalysts had distinguishable metallic Ni peaks, while the peaks were barely observed throughout the reaction for the NiO(4nm)-containing catalyst. These results indicate that the crystallite size of Ni in NiO(4nm) is smaller than those in NiO(36nm) and NiO(101nm). In addition, the catalysts exhibited different MoCx evolution characteristics. In the case of NiO(36nm)- and NiO(101nm)-containing catalysts, the Mo_2C peak was not observed for either the pretreated or post-reaction catalysts, indicating that the Mo_2C species were highly dispersed in the samples. However, the Mo_2C peak appeared in the Mo/HZSM-5 and NiO(4nm)-Mo/HZSM-5 spectra, revealing that Mo_2C agglomeration was more significant in these samples.

Changes in the particle sizes of the Ni and Mo species in the pretreated and post-reaction samples were monitored by TEM. Table 2-4 lists the average particle sizes of the catalysts and the corresponding TEM-EDS images of the pretreated and post-reaction samples are shown in Figures 2-5 and 2-6, respectively. After the pretreatment process, the metallic Ni sizes of NiO(4nm)-Mo/HZSM-5 and NiO(36nm)-Mo/HZSM-5 increased from 4.5 nm to 28.9 nm and 35.7 nm to 49.3 nm, respectively. The NiO nanoparticles were vulnerable to sintering during the reduction process to minimize their

surface energy [33,42,43]. In contrast, the average particle size of NiO(101nm) decreased from 101.3 nm to 77.6 nm with a wide range of size distribution. The decrease in the bulk metal particle size was due to the particle destruction during oxygen removal, as observed via environmental TEM [44]. Although the size of the Ni particles changed after pretreatment, the order of the Ni particle size was maintained.

The Ni particle sizes of the post-reaction catalysts were different from those of the pretreated catalysts. Compared to the pretreated catalysts, the particle size of Ni in NiO(4nm)-Mo/HZSM-5 increased to 31.6 nm, whereas those of NiO(36nm)-Mo/HZSM-5 and NiO(101nm)-Mo/HZSM-5 decreased to 41.1 nm and 44.4 nm, respectively, after the reaction. Different evolution mechanisms of Ni particles, depending on their size, have been reported in previous studies of methane decomposition [42,43]. According to a previous study, small Ni particles with crystallite sizes below 25 nm merge to acquire thermodynamic stability, whereas Ni crystallites larger than 30 nm split into smaller fragments owing to carbon deposition [42]. Several studies have proposed kinetic modeling for carbon growth on Ni, suggesting that deposited surface carbon diffuse through the bulk Ni particles, splitting large Ni particles until they are completely covered with the graphite layer [43,45,46]. Therefore, it can be inferred that the size of Ni particles in NiO(4nm) increased owing to stabilization, whereas those in NiO(36nm) and NiO(101nm) decreased owing to carbon diffusion inside the particles.

Furthermore, the particle size of external MoCx varied depending on the

NiO particle size. When NiO(36nm)-Mo/HZSM-5 and NiO(101nm)-Mo/HZSM-5 were used, the external MoCx particles of the pretreated and post-reaction catalysts were smaller than those of Mo/HZSM-5 and NiO(4nm)-Mo/HZSM-5. This indicates higher MoCx dispersion on NiO(36nm)-Mo/HZSM-5 and NiO(101nm)-Mo/HZSM-5, which is consistent with the XRD results. External Mo_2C is an inactive species for MDA and causes low methane conversion [47]. This evidence demonstrates that the higher conversion of NiO(36nm)-Mo/HZSM-5 and NiO(101nm)-Mo/HZSM-5 is attributed to the lower agglomeration of Mo_2C on the external surface. However, there were limitations in measuring the size of MoCx using TEM, in which only external MoCx could be observed, and the accumulated coke on MoCx could not be distinguished individually.

To compare the dispersion of both external and internal MoCx species, CO chemisorption experiments were conducted (Table 2-5). First, the CO chemisorption of the reduced NiO(Xnm)-HZSM-5 samples without Mo species was conducted. It was confirmed that CO adsorption on Ni was not observed even at the smallest size, i.e., NiO(4nm), probably because of its low content. Next, CO uptake was measured for the catalysts collected after the pretreatment step. The CO uptakes of Mo/HZSM-5 and NiO(4nm)-Mo/HZSM-5 were 0.056 and 0.063 mmol/g_{cat}, respectively. NiO(36nm)-Mo/HZSM-5 had the largest CO adsorption of 0.091 mmol/g_{cat}, and NiO(101nm)-Mo/HZSM-5 had a slightly lower CO adsorption of 0.078 mmol/g_{cat}. In the case of the post-reaction samples, the CO uptakes

decreased compared to those of their pretreated counterparts. Nevertheless, when NiO(36nm)-Mo/HZSM-5 and NiO(101nm)-Mo/HZSM-5 were used, the CO uptakes were higher than those of Mo/HZSM-5 and NiO(4nm)-Mo/HZSM-5. As CO uptake is positively correlated with the MoCx dispersion [28,48], it can be inferred that the MoCx dispersion is higher on NiO(36nm)-Mo/HZSM-5 and NiO(101nm)-Mo/HZSM-5 than on Mo/HZSM-5 and NiO(4nm)-Mo/HZSM-5, which is in good agreement with the previous XRD and TEM results. Hence, it can be concluded that the higher MoCx dispersion, which is induced by the presence of NiO(36nm) and NiO(101nm), accounts for the enhanced reactivities of NiO(36nm)-Mo/HZSM-5 and NiO(101nm)-Mo/HZSM-5.

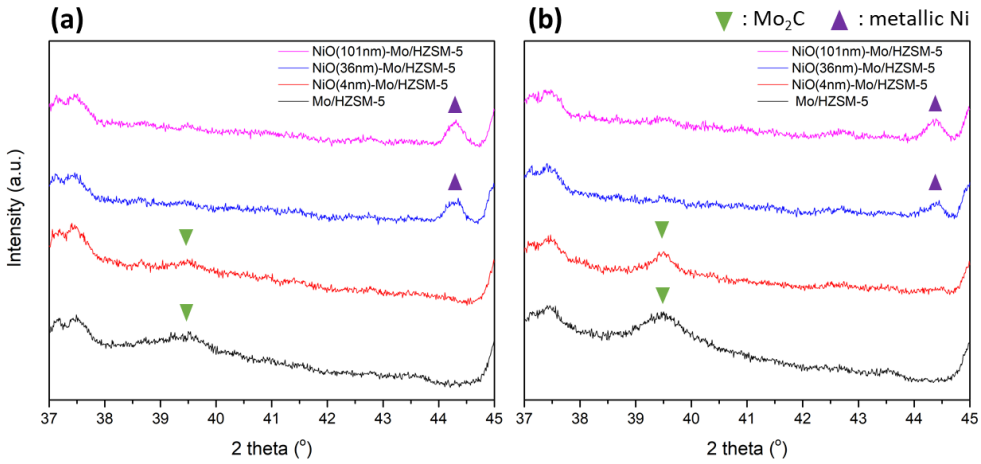

Figure 2-4. XRD patterns of pretreated NiO(X)-Mo/HZSM-5 (a), and post-reaction NiO(X)-Mo/HZSM-5 (b) with various NiO particle size.

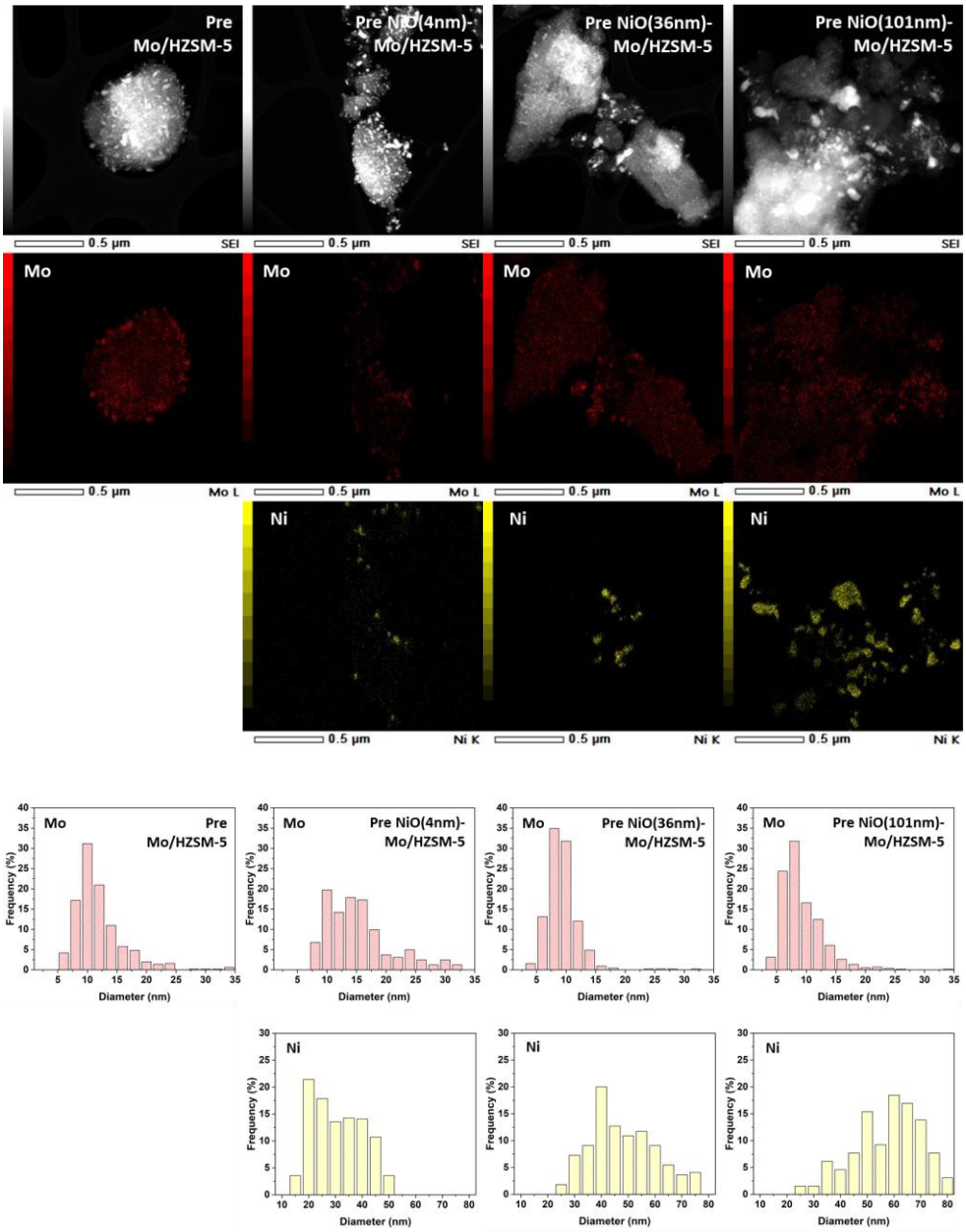

Figure 2-5. TEM-EDS images of pretreated samples and corresponding size distributions.

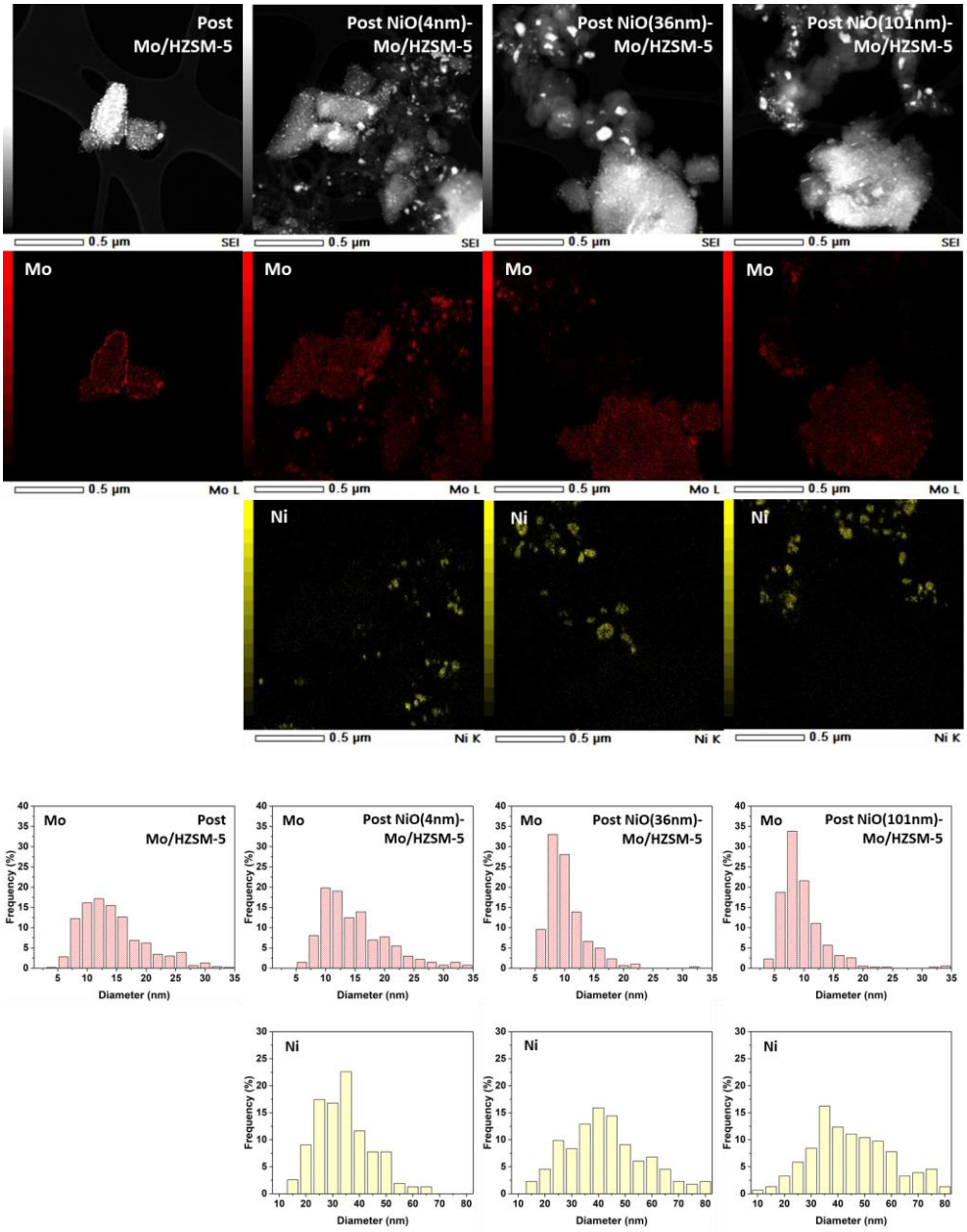

Figure 2-6. TEM-EDS images of post-reaction samples and corresponding size distributions.

Table 2-4. Average particle size of Ni and MoCx on catalysts after the pretreatment or the reaction.

Catalyst		Average particle size[a] (standard deviation)	
		Ni	MoCx[b]
Pretreated	Mo/HZSM-5	-	12.2 (7.8)
	NiO(4nm)-Mo/HZSM-5	28.9 (10.3)	14.3 (5.5)
	NiO(36nm)-Mo/HZSM-5	49.3 (16.4)	8.4 (3.3)
	NiO(101nm)-Mo/HZSM-5	77.6 (40.3)	8.2 (3.5)
Post-reaction	Mo/HZSM-5	-	13.9 (6.5)
	NiO(4nm)-Mo/HZSM-5	31.6 (10.4)	15.3 (8.9)
	NiO(36nm)-Mo/HZSM-5	41.1 (16.3)	9.6 (4.8)
	NiO(101nm)-Mo/HZSM-5	44.4 (19.2)	9.0 (5.3)

a: Determined by TEM analysis, unit: nm

b: External MoCx + Coke accumulated on MoCx

Table 2-5. CO uptake of catalysts after the induction period.

Catalyst		CO uptake (mmol/g_{cat})
Pretreated	Mo/HZSM-5 [a]	0.056
	NiO(4nm)-Mo/HZSM-5 [a]	0.063
	NiO(36nm)-Mo/HZSM-5 [a]	0.091
	NiO(101nm)-Mo/HZSM-5 [a]	0.078
Post-reaction	Mo/HZSM-5 [a]	0.042
	NiO(4nm)-Mo/HZSM-5 [a]	0.048
	NiO(36nm)-Mo/HZSM-5 [a]	0.087
	NiO(101nm)-Mo/HZSM-5 [a]	0.070
	NiO(4nm)-HZSM-5 [b]	0
	NiO(36nm)-HZSM-5 [b]	0
	NiO(101nm)-HZSM-5 [b]	0

a: Reduced at 700 ℃ in H_2 for removal of passivation layer

b: Reduced at 700 ℃ in H_2 for NiO reduction

2.3.4. Reducibility of catalysts (CH_4–TPR)

To investigate the reducibility of the NiO particles, CH_4–TPR was conducted on bulk NiO (Figure 2-7). When NiO was reduced, the CO_2 and H_2 peaks were simultaneously generated as a result of CH_4 consumption. The reduction temperature decreased as the particle size decreased as follows: NiO(4nm) at 403 °C, NiO(36nm) at 466 °C, and NiO(101nm) at 576 °C. At higher temperatures, only H_2 was produced, whereas benzene was not detected, indicating that metallic Ni converted methane to coke without producing benzene. The reduction temperature of NiO was consistent after mixing NiO with HZSM-5 (Figure 2-8), indicating that there was no severe sintering owing to physical mixing. Benzene was not produced over NiO-HZSM-5, revealing that NiO only acts as a promotor and is not involved in the generation of aromatic hydrocarbons from CH_4.

The reduction sequence of the metal oxides on the catalysts during the pretreatment step is shown in Figure 2-9. In the case of Mo/HZSM-5, MoO_3 started to reduce to MoO_2 at 640 °C, as evidenced by the evolution of the H_2 and CO peaks. The reduction peak that corresponds to the change of MoO_2 to MoCx appeared at 675 °C, followed by the production of benzene, which started to form at 685 °C. These results imply that MoCx is the active phase for benzene production [49,50].

An additional reduction peak was observed below 600 °C over NiO(36nm)-Mo/HZSM-5. The peak located at 538 °C was attributed to the reduction of NiO to metallic Ni and MoO_3 to MoO_2. The MoCx formation

caused by the MoO_2 reduction occurred at 633 °C, which was 42 °C lower than the MoCx formation temperature of Mo/HZSM-5. Owing to the decrease in the MoCx formation temperature, the benzene production temperature also decreased by 41 °C compared with that of Mo/HZSM-5. As the Tamman temperatures of MoO_3, MoO_2, and Mo_2C are 261 °C, 414 °C, and 1,209 °C, respectively, the transformation of MoO_3 to MoO_2 or MoO_2 to MoCx at lower temperatures restricts the agglomeration of Mo species [28,51]. Therefore, lowering the MoOx reduction temperature enhanced the MoCx dispersion, which was confirmed by XRD, TEM, and CO chemisorption. This phenomenon explains the highest MoCx dispersion of NiO(36nm)-Mo/HZSM-5, which had the lowest reduction temperatures of NiO and MoOx.

NiO(101nm)-Mo/HZSM-5 had a higher reduction temperature of metal oxides than NiO(36nm)-Mo/HZSM-5 as follows: NiO to metallic Ni and MoO_3 to MoO_2 at 576 °C and MoO_2 to MoCx at 636 °C. The higher reduction temperatures of the Ni and Mo species are attributed to the higher reduction temperature of bulk NiO(101nm). However, the NiO reduction temperature of NiO(4nm)-Mo/HZSM-5 was the highest, which is different from the CH_4–TPR results for bulk NiO. Interestingly, both NiO and MoOx reduction peaks appeared simultaneously at 658 °C. The higher C_6H_6 production temperature of 682 °C was a consequence of the delayed reduction of NiO and MoOx. In addition, it appears that the lower dispersion of MoCx, which was discussed in Section 3.3, originates from

the higher reduction temperatures of the metal oxides.

Notably, the reduction temperature of NiO changed after physical mixing with Mo/HZSM-5. The change became significant as the size of NiO particles decreased; the reduction temperatures of NiO(4nm) and NiO(36nm) increased by 255 °C and 72 °C, respectively, while the reduction temperature of NiO(101nm) remained unchanged. In the case of NiO(36nm), increasing the NiO reduction temperature did not inhibit the reduction of MoOx. Meanwhile, the reduction temperature of NiO(4nm) increases substantially, suppressing the reduction of MoOx. This phenomenon was only observed in the presence of Mo, which indicates that the transition of the NiO reduction temperature can be attributed to the interaction between NiO and Mo species.

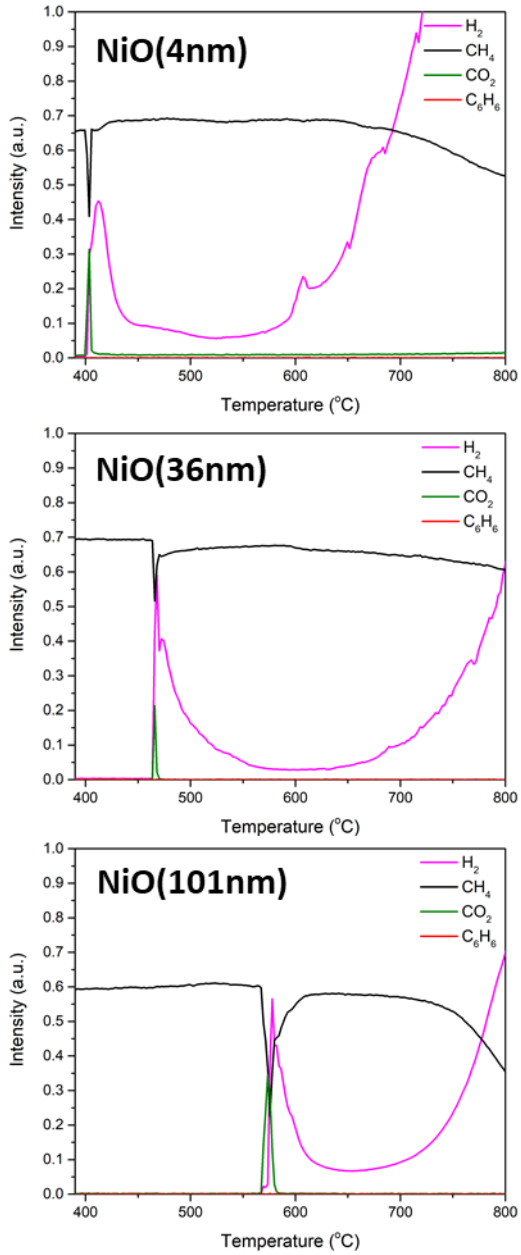

Figure 2-7. CH_4–TPR results of bulk NiO with various sizes of NiO.

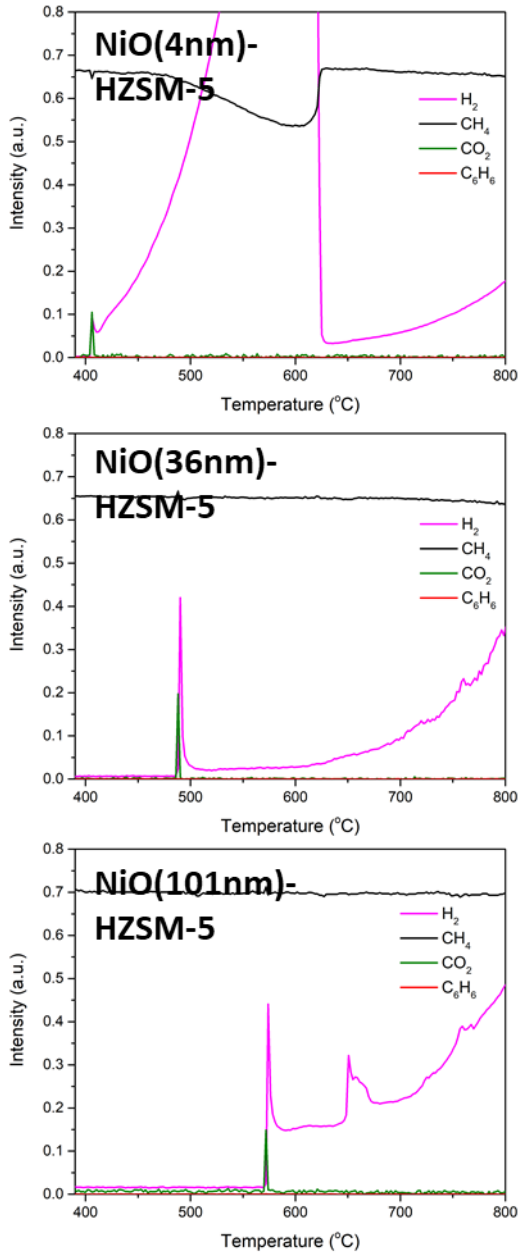

Figure 2-8. CH_4–TPR results of NiO(X)-HZSM-5 with various sizes of NiO.

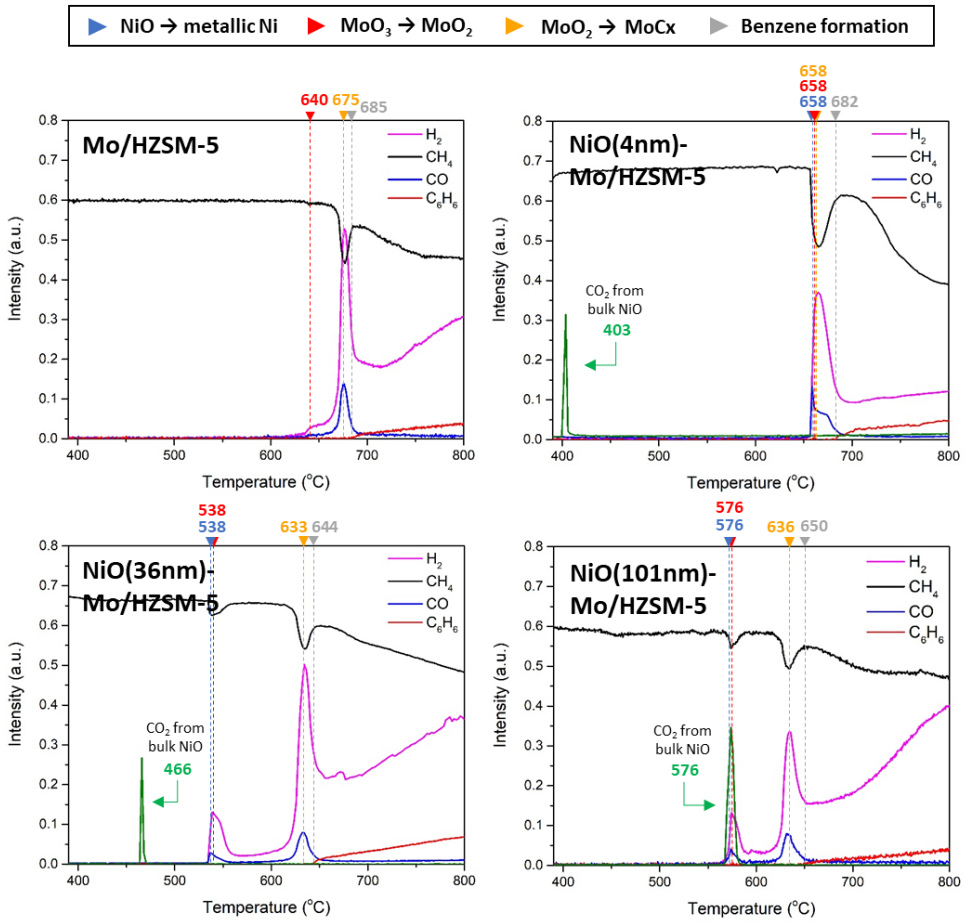

Figure 2-9. CH_4–TPR results of NiO(X)-Mo/HZSM-5 with various sizes of NiO.

2.3.5. Interaction between NiO and MoOx in reducing atmosphere

To examine the reason for the transition of the NiO reduction temperature, additional CH_4–TPR experiments were conducted on NiO(101nm)-Mo/HZSM-5, in which the NiO reduction temperature was not shifted. Table 2-6 lists the CH_4–TPR reduction temperatures of the metal oxides on NiO(101nm)-Mo/HZSM-5 with different NiO and MoOx contents. First, the Ni:Mo ratio was changed by doubling the NiO content in the catalyst to examine whether the reducibility of the catalyst was altered when the total surface area of NiO particles in contact with MoOx increased (Figure 2-10). When the NiO content was doubled, no peak shift was observed, implying that the total surface area of the NiO particles did not affect the interaction with MoOx. However, when the NiO and Mo contents were simultaneously doubled, the reduction temperatures of NiO and MoO_3 increased to 608 °C. Nevertheless, the reduction temperature of MoO_2 was not altered significantly, probably because the reduction of MoO_3 occurred below 610 °C, which was not sufficiently high to hinder the reduction of MoO_2. Although NiO(1wt.%)-Mo(12wt.%)/HZSM-5 and NiO(2wt.%)-Mo(24wt.%)/HZSM-5 had the same Ni:Mo ratio, reduction peaks of NiO and MoO_3 shifted to high temperatures when the Mo content increased. As only a limited amount (approximately 5 %) of Mo could be impregnated inside zeolite pores [52], the content of external MoO_3 species rapidly increased when the Mo content increased. Therefore, it can be inferred that the amount of external MoO_3 increased over NiO(2wt.%)-

Mo(24wt.%)/HZSM-5, and external MoO_3 inhibited the reduction of NiO.

To verify that the external MoO_3 species caused a shift in the reduction temperature, additional MoO_3 powder was added to NiO(1wt.%)-Mo(12wt.%)/HZSM-5 by physical mixing (Figure 2-11). When 1 wt.% and 5 wt.% of MoO_3 were added, the reduction temperatures increased to 597 °C and 610 °C, respectively. These results suggest that the reduction peaks shifted to higher temperatures because of the interaction between NiO particles and the external MoO_3. In the previous CH_4–TPR results, the reduction temperature of NiO(4nm) was 403 °C in the bulk phase, and it increased to 658 °C when NiO(4nm) was physically mixed with Mo/HZSM-5. Therefore, it can be concluded that the transition in the reduction temperature resulted from the interaction between NiO(4nm) and the external MoO_3. In addition, our results suggest that it is much easier for the smaller NiO particles to interact with the external MoO_3 species.

In situ XRD was performed on the NiO(1wt.%)-Mo(12wt.%)/HZSM-5 catalyst to understand how two metal oxides on the external surface interact during the pretreatment procedure (Figure 2-12). Before analyzing the NiO-containing samples, the phase evolution of Mo/HZSM-5 was analyzed from 25 °C to 650 °C. A prominent MoO_3 peak at 27.40°, which is attributed to external MoO_3, was observed up to 550 °C, and the MoO_2 phase appeared at 650 °C, which is in good agreement with the CH_4–TPR result. For NiO(36nm)-Mo/HZSM-5 and NiO(101nm)-Mo/HZSM-5, there was no phase transition observed below 450 °C. At 550 °C, the NiO and MoO_3

peaks were partly reduced, and a new peak at 26.64° corresponding to the $NiMoO_4$ phase was observed. This indicates that some amount of NiO formed an alloy with MoO_3 during the pretreatment step, even though they were physically mixed. It has been reported that the $NiMoO_4$ phase can be formed by reducing a mixture of NiO and MoO_3 powder [53-55]. When the temperature was increased to 650 °C, NiO was completely reduced to metallic Ni, and certain graphite-2H peaks could be observed. It is well established that $NiMoO_4$ is separated into metallic Ni and MoO_2 and finally converted to metallic Ni and MoCx during carburization [53-55]. Therefore, $NiMoO_4$ was probably separated into metallic Ni and MoCx at 650 °C, although the MoCx phase could not be detected at 650 °C.

However, the $NiMoO_4$ phase was detected from 450 °C to 550 °C in the case of the NiO(4nm)-Mo/HZSM-5 sample. While the MoO_3 phase of the NiO(36nm)-Mo/HZSM-5 and NiO(101nm)-Mo/HZSM-5 samples remained at 550 °C, the MoO_3 phase disappeared, and only the $NiMoO_4$ phase was detected in the NiO(4nm)-Mo/HZSM-5 sample. The evolution of the $NiMoO_4$ phase was more clearly observed when the NiO content in the catalyst was increased to 5 wt.% (Figure 2-13). The $NiMoO_4$ alloy phase was produced from NiO(4nm) and MoO_3 at 450 °C, while NiO(36nm) and NiO(101nm) formed the alloy at 550 °C. Based on the CH_4–TPR results (Figure 2-9), the increase in the reduction temperature of NiO(4nm) could be explained by the formation of $NiMoO_4$. In addition, it is clear that the $NiMoO_4$ formation is facilitated as the NiO particle size decreases. On the

other hand, a large peak at 650 °C assigned to the MoO_2 phase was observed for NiO(4nm)-Mo/HZSM-5. It appears that MoO_2 agglomeration was attributed to the $NiMoO_4$ formation. As indicated by the CH_4–TPR results, the majority of MoO_3 species in NiO(4nm)-Mo/HZSM-5 formed $NiMoO_4$, and the $NiMoO_4$ phase was separated to metallic Ni and MoO_2 at the higher temperature, suppressing the dispersion of MoO_2. In addition, the MoO_2 agglomeration could account for the low MoCx dispersion, as observed in the XRD, TEM, and CO chemisorption analyses.

To examine the effect of $NiMoO_4$ on Mo/HZSM-5, bulk $NiMoO_4$ was physically mixed with Mo/HZSM-5, and its catalytic activity is shown in Figure 2-14. The Ni content in $NiMoO_4$-Mo/HZSM-5 was identical to that in the NiO-Mo/HZSM-5 catalyst. The methane conversion of $NiMoO_4$-Mo/HZSM-5 was higher than that of NiO(4nm)-Mo/HZSM-5, probably because additional Mo species from the $NiMoO_4$ converted methane. However, as additional Mo species may be located on the external surface, the BTX selectivity of $NiMoO_4$-Mo/HZSM-5 was lower than that of NiO(4nm)-Mo/HZSM-5. As a result, $NiMoO_4$-Mo/HZSM-5 had BTX yields of 4.7 % and 2.1 % at 40 min and 840 min, respectively, which were similar to those of NiO(4nm)-Mo/HZSM-5, in which $NiMoO_4$ was dominantly formed during the reduction process. This result confirms that $NiMoO_4$ is the inactive phase for the MDA reaction using the NiO-Mo/HZSM-5 catalyst.

However, as in-situ XRD results and MDA activity of $NiMoO_4$-

Mo/HZSM-5 could only explain the interaction between Ni and Mo species at the external surface, the interaction inside the pore was further investigated. If there was the interaction between those metals inside the pore, diffusion of Ni into the pore should have occurred during the reaction. Therefore, the possibility of Ni diffusion into the pore was investigated by line-EDS. Figure 2-15 shows line EDS images of pretreated NiO(4–101nm)-Mo/HZSM-5. The line could be divided into the zeolite region where the Si was present, and the non-zeolite region. In the non-zeolite region, external Ni particles were observed which was covered with coke. Interestingly, small amount of Mo was detected on Ni particles in the non-zeolite region, and the intensity increased as particle size of Ni decreased. This indicates that external Mo interacted with Ni more severely as the size of Ni decreased, which was verified by CH_4-TPR (Figure 2-9) and in-situ XRD results (Figure 2-12). Meanwhile, in the zeolite region, intensity of Ni was much lower than the intensity at the non-zeolite region. If significant amount of Ni was dispersed in zeolite pore, the intensity in the zeolite region would be higher. Therefore, it can be seen that the amount of Ni dispersed in the pore was insignificant, and most of Ni was present at the external surface.

In addition, N_2 physisorption was conducted to examine whether Ni was dispersed in the pores after the reduction (Table 2-7). If Ni was dispersed in zeolite pores when the catalyst was reduced, the specific surface area would decrease. However, if NiO-Mo/HZSM-5 catalysts are analyzed, the

difference of porosity induced by Ni or Mo could not be distinguished. Therefore, N_2 physisorption was conducted on NiO-HZSM-5, a catalyst in which NiO was physically mixed with HZSM-5. In addition, the smaller the size of NiO, the more easily ripening occurs, so NiO(4nm)-HZSM-5 was analyzed as a representative. For a comparison, NiO-HZSM-5 (IMP) was prepared by impregnation, assuming that Ni was highly dispersed into the pore of NiO-HZSM-5 (IMP). Prior to N_2 physisorption, all samples were reduced by exposure to 700 ^{o}C in H_2 atmosphere. The reason for reducing to H_2 instead of CH_4 is that since coke is generated when reducing with CH_4, it is impossible to distinguish whether the decrease in surface area is due to Ni or coke. Therefore, BET surface area of reduced HZSM-5, NiO(4nm)-HZSM-5 and NiO-HZSM-5 (impregnated sample) were compared. As a result, the surface area of NiO(4nm)-HZSM-5 decreased to 324.4 m^2g^{-1} (2.6 % decrease compared to HZSM-5). However, in the case of NiO-HZSM-5 (IMP), the BET surface area was reduced to 309.2 m^2g^{-1} (7.2 % decrease compared to HZSM-5). It can be seen that the decrease in BET surface area was smaller in NiO(4nm)-HZSM-5 than NiO-HZSM-5 (IMP). Therefore, it can be concluded that the amount of Ni dispersed into the pores after reduction was insignificant.

In our previous study [29], the MDA performance was evaluated over NiO-Mo/HZSM-5 (IMP) which was prepared by co-impregnation, and NiO-Mo/HZSM-5 (PM) which was prepared by the physical mixing of NiO(101nm) and Mo/HZSM-5. Promoting effect of Ni was not found over

bimetallic NiO-Mo/HZSM-5 (IMP), indicating that even if a small amount of Ni was dispersed into the pores to form bimetallic Mo-Ni phase, it would inhibit catalytic stability. Therefore, it is important for Ni to exist on the external surface so that Ni and Mo do not form bimetallic phase.

It can be summarized that as the size of NiO decreased, it was more likely to interact with the external Mo species by forming the inactive $NiMoO_4$ phase. For the NiO(4nm)-Mo/HZSM-5 sample, NiO(4nm) was susceptible to producing $NiMoO_4$, thereby increasing the reduction temperature of NiO by 255 °C. Such a severe temperature shift resulted in a higher reduction temperature for MoOx and a lower MoCx dispersion. In contrast, NiO(101nm) barely interacted with MoO_3, and the reduction temperature of NiO(101nm) was identical to that of its bulk state. Therefore, metallic Ni, which was reduced before MoO_3, facilitated the reduction and dispersion of MoOx. Finally, in the case of NiO(36nm)-Mo/HZSM-5, a small fraction of NiO particles smaller than 20 nm was present in the sample, as shown in Figure 2-2. These small NiO particles may have formed $NiMoO_4$ when they were mixed with Mo/HZSM-5, causing an increase in the reduction temperature of NiO(36nm) by 72 °C. However, the NiO particles that did not interact with MoO_3 were reduced to metallic Ni at the lowest temperature, which was active for the earlier reduction of MoOx. Therefore, the reduction temperature of MoOx decreased the most, leading to the highest dispersion and catalytic activity. As NiO(36nm) has the smallest particle size among the NiO samples which are less prone to form

inactive $NiMoO_4$, NiO(36nm) was concluded to be the optimal size for promoting Mo/HZSM-5 catalyst in the MDA reaction.

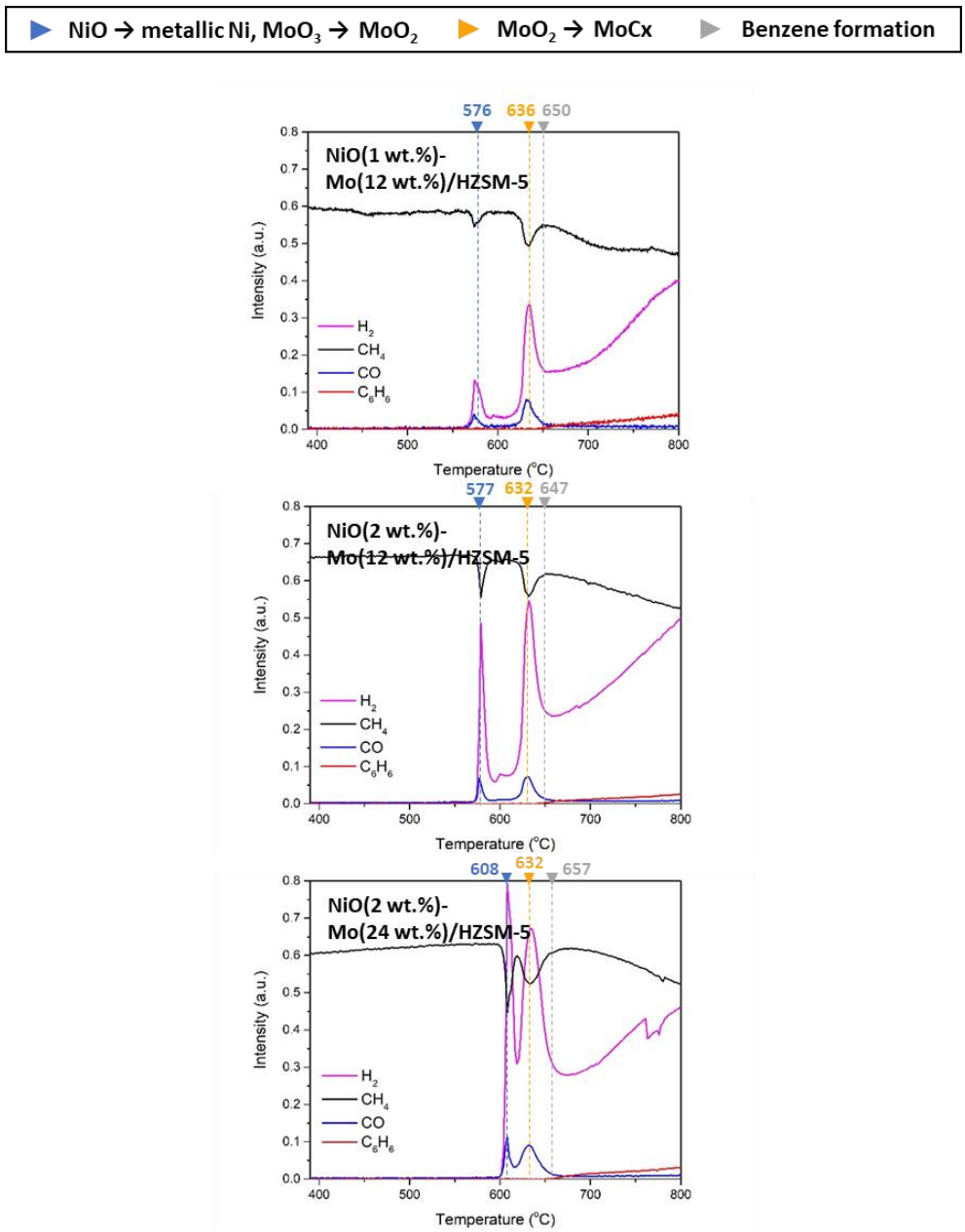

Figure 2-10. CH_4–TPR results of NiO(101nm)-Mo/HZSM-5 catalysts with various Ni:Mo ratios.

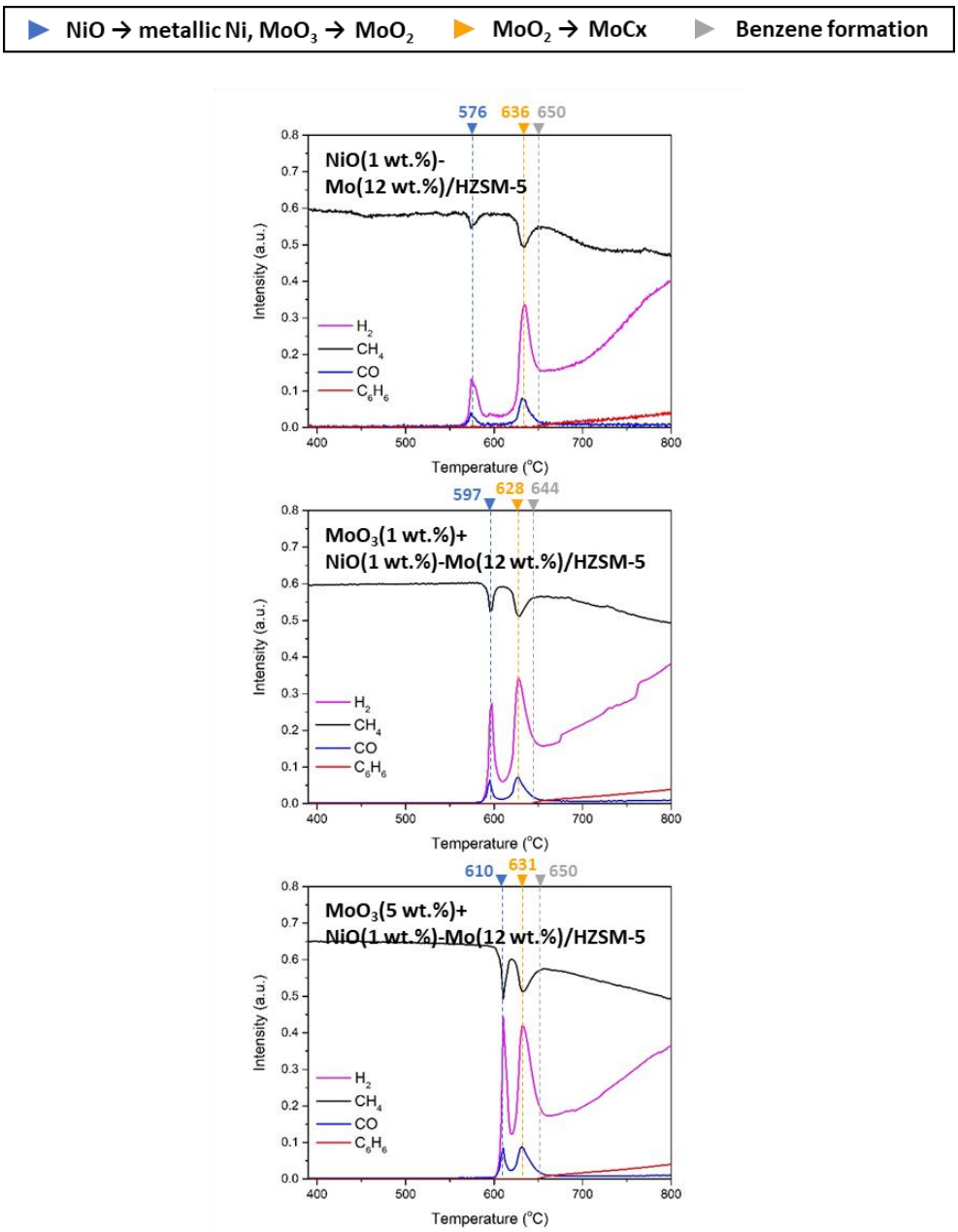

Figure 2-11. CH_4–TPR results of MoO_3 added NiO(101nm)-Mo/HZSM-5 catalysts.

Table 2-6. Reduction temperature of metal oxides and benzene formation temperature over catalysts during CH_4-TPR (unit: ^oC).

Catalysts (NiO: 101 nm)	NiO → metallic Ni MoO_3 → MoO_2	MoO_2 → MoC_x	C_6H_6
NiO(1wt.%)-Mo(12wt.%)/HZSM-5	576	636	650
NiO(2wt.%)-Mo(12wt.%)/HZSM-5	577	632	647
NiO(2wt.%)-Mo(24wt.%)/HZSM-5	608	632	657
MoO_3(1wt.%) + NiO(1wt.%)-Mo(12wt.%)/HZSM-5	597	628	644
MoO_3(5wt.%) + NiO(1wt.%)-Mo(12wt.%)/HZSM-5	610	631	650

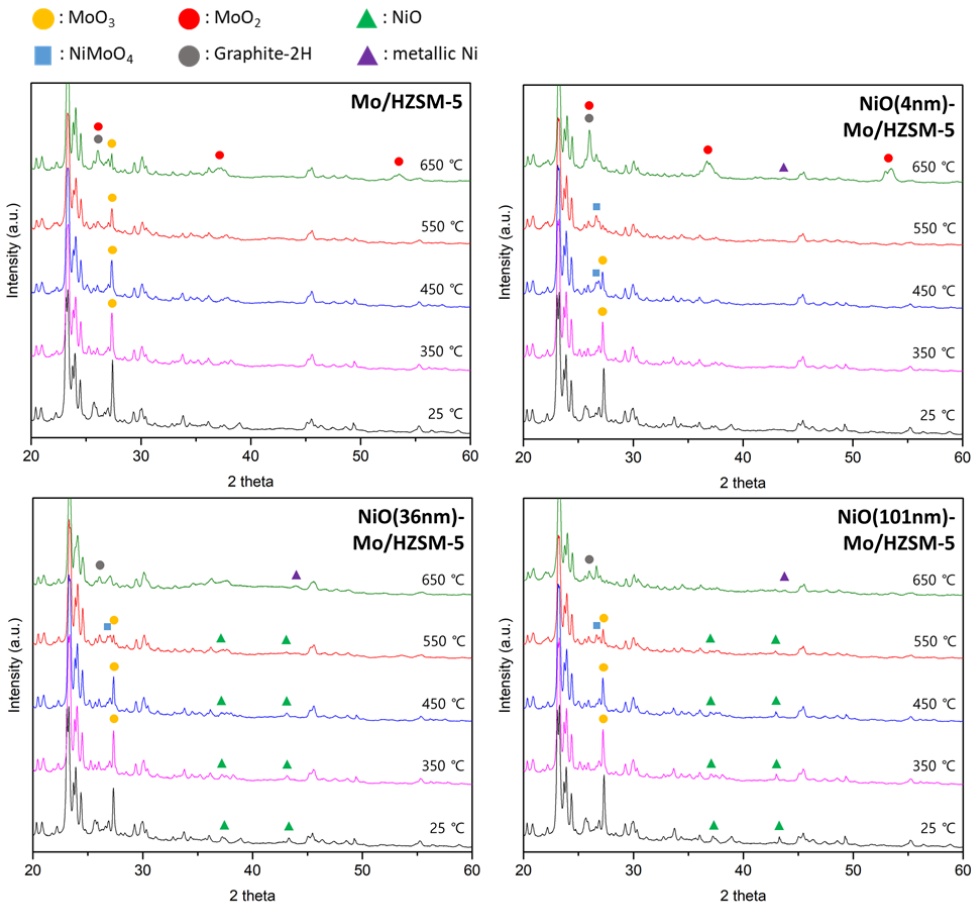

Figure 2-12. In-situ XRD patterns of NiO(1wt.%)-Mo(12wt.%)/HZSM-5 catalysts with various NiO particle size.

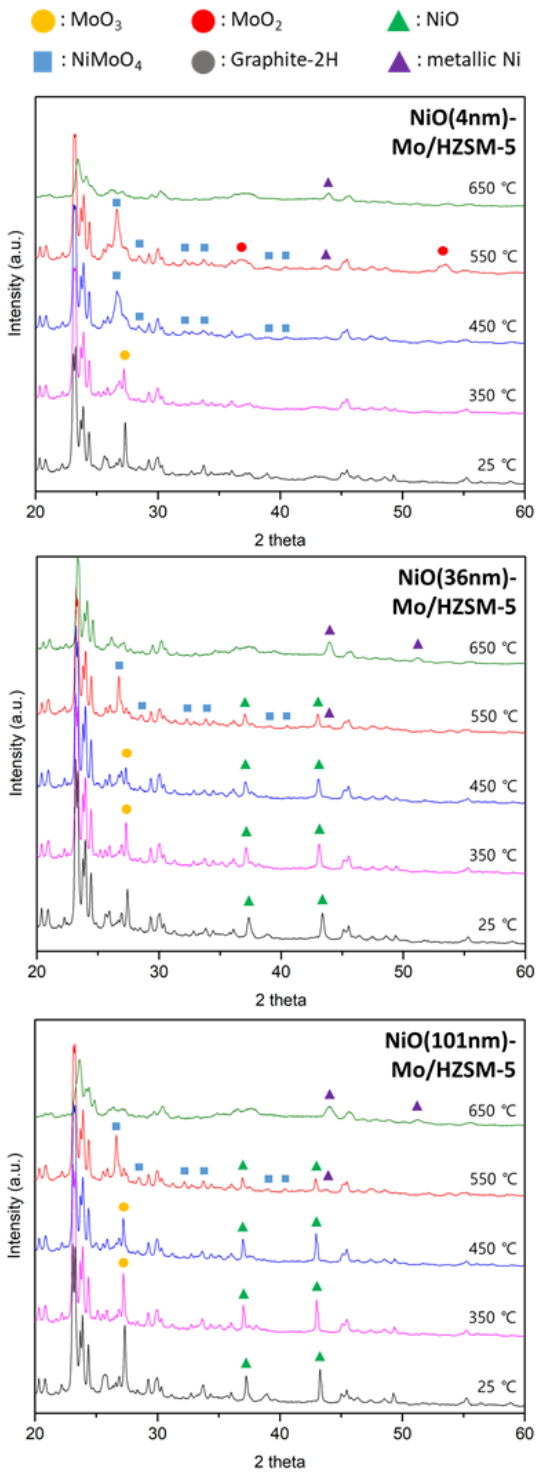

Figure 2-13. In-situ XRD patterns of NiO(5wt.%)-Mo(12wt.%)/HZSM-5 catalysts with various NiO particle size.

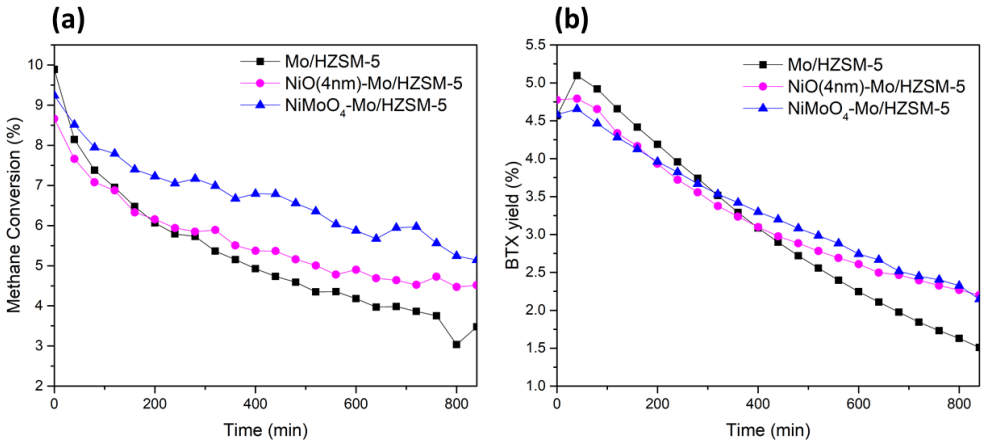

Figure 2-14. Catalytic performance of $NiMoO_4$-Mo/HZSM-5 and NiO(4nm)-Mo/HZSM-5

: (a) Methane conversion, and (b) BTX yield.

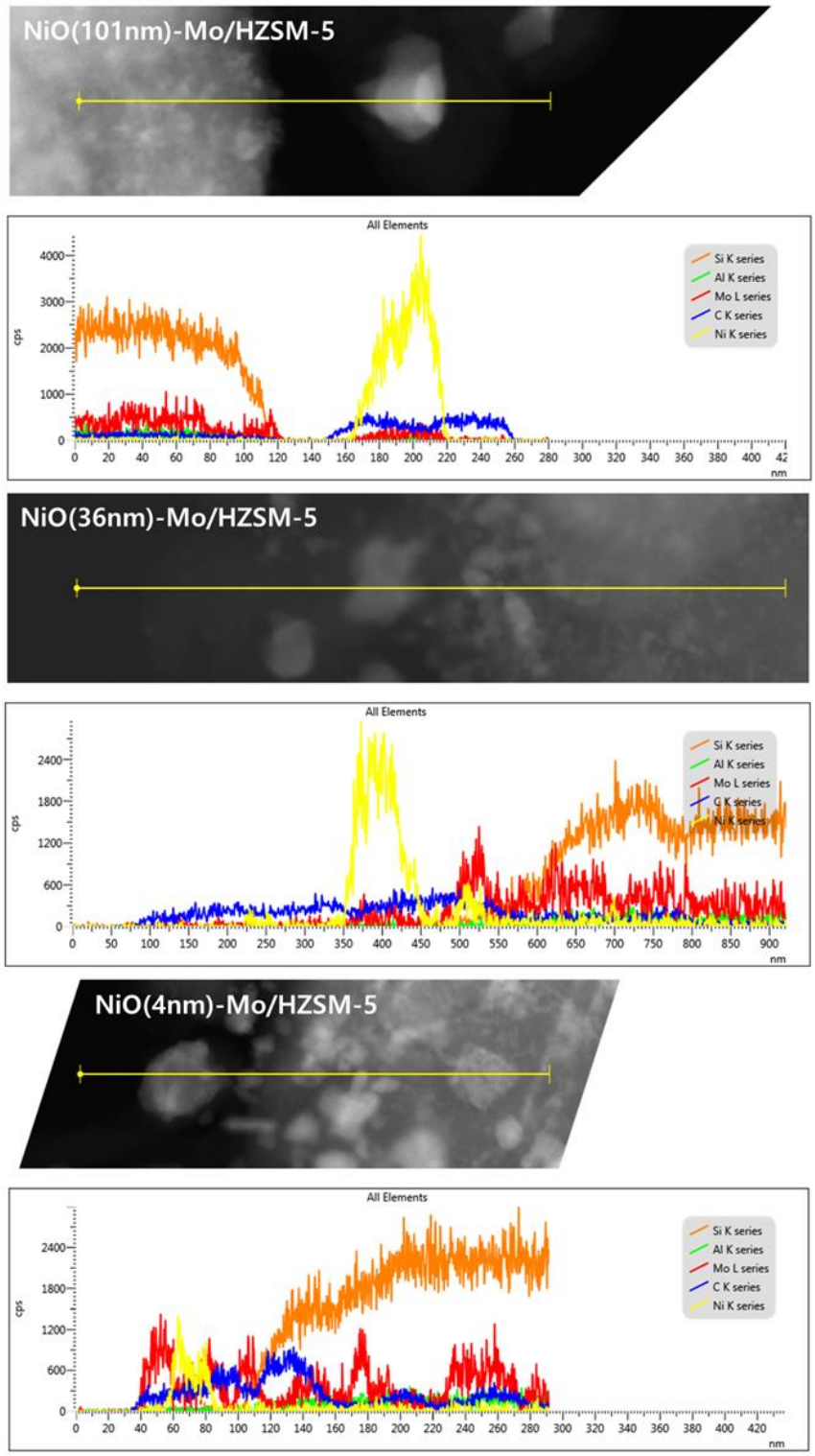

Figure 2-15. Line EDS images of pretreated NiO-Mo/HZSM-5 samples.

Table 2-7. N_2 physisorption results of reduced catalysts.

Catalyst	S_{BET} (m^2g^{-1})
HZSM-5	333.2
NiO(4nm)-HZSM-5[a]	324.4
NiO-HZSM-5 (IMP)[a]	309.2

a: Content of NiO in the catalyst: 1 wt.%, which is equivalent to the amount of NiO in NiO-Mo/HZSM-5.

2.3.6. Coke distribution of post-reaction catalysts

The amount and type of coke deposited on the post-reaction catalysts were analyzed according to the NiO particle size. Table 2-8 lists the peak areas of the individual coke species obtained from the TPO profiles (Figure 2-16). The TPO profiles were deconvoluted into four peaks centered at 437–471 °C, 493–504 °C, 541–548 °C, and 575–593 °C. The three peaks under 575 °C were assigned to low-temperature coke (LT coke), middle-temperature coke (MT coke), and high-temperature coke (HT coke). These peaks showed similar TPO patterns as those observed in previous studies of Mo/HZSM-5 [56,57]. According to previous studies [56,57], LT coke corresponds to reactive surface carbon deposits. MT and HT cokes are attributed to the graphite-like coke on the external surface and the polyaromatic coke inside the zeolite channels, respectively. The peak at the highest temperature, which was only observed in NiO-containing catalysts, was attributed to CNT, whose formation was induced by metallic Ni [26,29].

Compared with the NiO-containing samples, the post-reaction Mo/HZSM-5 sample had the largest amounts of LT and HT cokes. Because LT coke is a highly reactive species [57], its effect on catalyst deactivation has not been reported. Meanwhile, HT coke was revealed to be the main coke species, contributing to rapid catalyst deactivation [57]. Therefore, the high deactivation rate of Mo/HZSM-5 could be ascribed to the largest amount of HT coke formed.

The amount of MT coke and CNT was influenced by the NiO particle

size. When NiO(4nm) was added, the amount of MT coke and CNT increased compared with that of Mo/HZSM-5, which agrees well with the higher coke selectivity of the reaction over NiO(4nm)-Mo/HZSM-5. The post-reaction NiO(4nm)-Mo/HZSM-5 sample had the highest MT coke content, demonstrating that it facilitated the production of external graphite-like coke. It has been reported that when Ni is promoted with MoCx, the carbon yield increases significantly during methane decomposition [58,59], and the unsupported bimetallic Ni-Mo catalyst can be encapsulated by carbon instead of producing CNT [60]. Therefore, a considerable amount of external coke in the post-reaction NiO(4nm)-Mo/HZSM-5 could be attributed to the synergetic coke formation induced by external Ni and MoCx.

As the NiO particle size increased, the amount of MT coke decreased, while the amount of CNT increased. It could be assumed that the Ni particles that did not interact with MoCx formed the CNT-type coke. The production of CNT inhibits coke formation on the active sites of Mo/HZSM-5 [29], whereas carbonaceous coke covering the external surface accelerates catalyst deactivation [47]. This coke distribution is in good agreement with the selectivity data, where the selectivity of $C_{10}H_8$, the main precursor for coke species that leads to deactivation [61], decreased over NiO-containing catalysts. Therefore, it can be inferred that NiO(36nm) and NiO(101nm) hindered the coke formation by forming CNT, resulting in higher catalytic stability.

The visible Raman spectra (Figure 2-17) show the dominant coke species on the post-reaction catalysts. The post-reaction Mo/HZSM-5 sample exhibited features of amorphous carbon, such as a broad D peak at 1000–1490 cm^{-1}, a shifted G peak at 1605 cm^{-1}, and the absence of a 2D peak [47,62,63]. Coke on the external surface consists of not only graphitic carbon but also amorphous carbon [15,64]. In contrast, the post-reaction NiO(101nm)-Mo/HZSM-5 had the characteristics of CNT, exhibiting a D peak at 1338 cm^{-1}, an asymmetric G peak at 1570 cm^{-1}, and a symmetric 2D peak at 2676 cm^{-1} [65,66]. As the NiO particle size increased, its spectrum resembled that of CNT, whereas as the size decreased, the spectrum exhibited features of amorphous coke. This shows that larger NiO particles prefer to produce CNT, which is consistent with the TPO profiles. In addition, catalysts with high stability featured CNT-type coke.

In summary, small NiO particles were susceptible to merging with external MoO_3 species, forming the $NiMoO_4$ phase, which was an inactive phase for the MoCx dispersion. After reduction, Ni and agglomerated MoCx on the external surface accelerated the production of external coke species. The external coke blocked the active site from beginning of the reaction, leading to rapid deactivation of the catalyst. In contrast, larger NiO particles were resistant to the formation of $NiMoO_4$; therefore, more MoCx could be dispersed inside the catalyst. As a result, the individual external Ni particles produced the CNT-type coke, which did not block the active sites of the catalysts and increased the catalytic stability of NiO(36nm)-Mo/HZSM-5

and NiO(101nm)-Mo/HZSM-5.

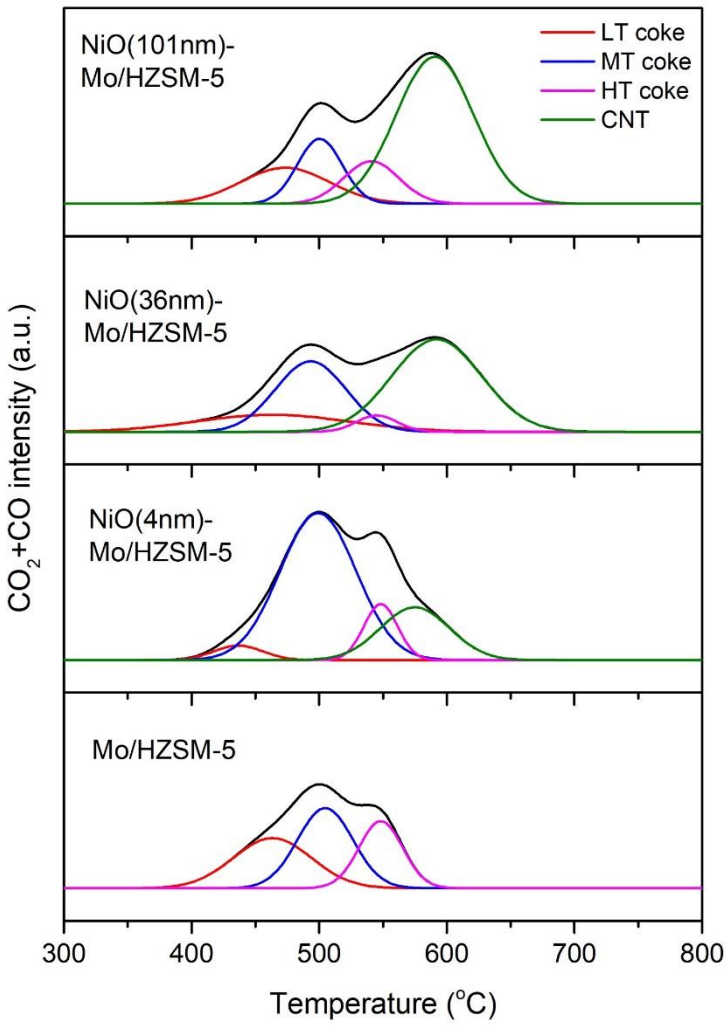

Figure 2-16. TPO profiles and corresponding deconvolution peaks of post-reaction catalysts.

Table 2-8. The coke amount of post-reaction catalysts estimated from peak area in TPO results (unit: a.u.).

Catalyst	LT coke	MT coke	HT coke	CNT
Mo/HZSM-5	5.9	6.7	4.4	-
NiO(4nm)-Mo/HZSM-5	1.1	16.8	2.9	5.5
NiO(36nm)-Mo/HZSM-5	3.9	7.5	1.0	12.4
NiO(101nm)-Mo/HZSM-5	4.8	4.4	3.5	17.1

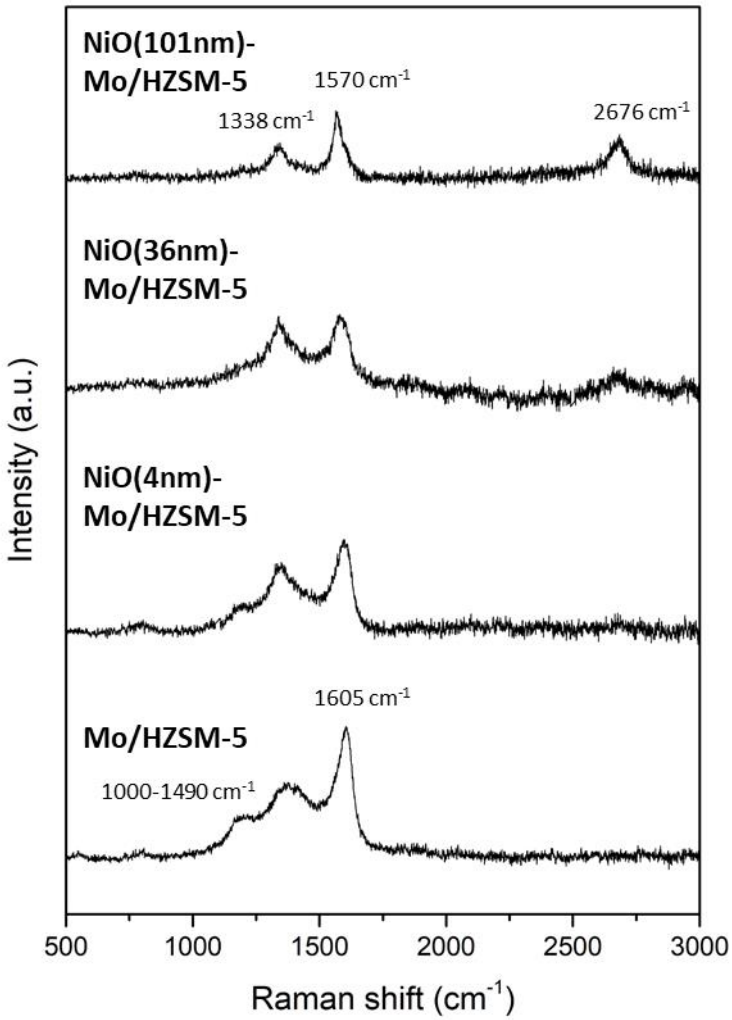

Figure 2-17. Raman spectra of post-reaction catalysts.

Chapter 3. CO_2 co-feeding Shale Gas Aromatization with Mg modified Mo/ZSM-5

3.1. Introduction

The production of shale gas, which is mainly composed of methane with trace amounts of ethane, propane, nitrogen, and carbon dioxide, is increasing rapidly [67-69]. Emission of greenhouse gases such as methane and carbon dioxide is increasing along with the massive production of shale gas [68]. It was reported that 0.42% of produced natural gas (2300 Gg of methane) is released into the atmosphere due to limitations in storage capacity and transportation infrastructure [70]. Converting shale gas to liquid hydrocarbons could be a promising solution because liquid hydrocarbons are facile for storage and transportation. Meanwhile, benzene, toluene, and xylene (BTX), which are the crucial building block of chemical products, have been produced from crude oil conventionally [1]. Therefore, producing BTX from shale gas is advantageous not only for reducing emission of greenhouse gases but also for finding alternative sources of BTX.

Non-oxidative dehydro-aromatization is an effective method for directly producing BTX and H_2 from light hydrocarbons. Its selectivity to benzene is between 60–80%, which makes this process attractive for benzene production [4]. Active metals ignite dehydrogenation of hydrocarbons, then

zeolites such as ZSM-5 and MCM-22 which have shape selectivity to BTX provide sites for oligomerization and aromatization [3,13,71]. Aromatization of a single hydrocarbon reactant has been widely studied [3,13,71], and co-aromatization of two hydrocarbons has also been investigated to overcome high activation energy of methane [4,6-8]. Also, shale gas, which is comprised of various hydrocarbons, could be used for aromatization [9,10] because higher yield of BTX could be obtained without the reactant separation.

Suitable catalyst for shale gas aromatization was investigated by Lim et al. [72], and molybdenum was found to be an optimum active metal owing to its ability to activate methane. At 750 ℃, yield of BTX reached its maximum over Mo/HZSM-5, but the catalyst was deactivated rapidly after 5 hr due to massive amount of coke [72]. In non-oxidative atmosphere, BTX could be easily polymerized to coke since coke is the most thermodynamically stable product [4]. Moreover, coke formation could be facilitated on free Brønsted acid sites as excess oligomerization proceeds on strong acid site [47,73,74]. In order to suppress coke formation, soft oxidant could be added to the feed, or catalyst could be modified to be resistant to coke.

CO_2 could be added as a soft oxidant in the feed to inhibit coke formation. Studies on CO_2 co-feeding methane aromatization reported that CO_2 led to slower deactivation attributed to continuous carbon removal via the Reverse Boudouard Reaction (Eq. 1) [75,76]. In addition, it was reported that CO

and H_2, which was produced from dry reforming reaction by CO_2 and CH_4 (Eq. 2), increased catalytic stability [5,77-79]. Especially, H_2 facilitated hydrogenation rates of surface carbon species, preventing coke formation [77,79].

$CO_2 + C^* \rightarrow 2CO + *$ (Eq.1)

$CO_2 + CH_4 \rightarrow 2CO + 2H_2$ (Eq.2)

From Eq.2, it should be noticed that co-feeding CO_2 with shale gas is advantageous not only to prevent coke formation but also to produce additional syngas [12]. Recently, Jung et al. studied the technoeconomic analysis of CO_2 co-feeding shale gas aromatization over Mo/ZSM-5 [12] and reported that when a methanol production process using syngas was integrated after the aromatization process, overall net present value (NPV) increased and CO_2 emission was significantly reduced. However, overall NPV of CO_2 co-feeding shale gas aromatization could be increased if catalytic performance is improved. Therefore, development of catalyst with higher activity and stability is necessary.

Catalyst could be modified by controlling the free Brønsted acid sites where coke is concentrated. Therefore, there were attempts to remove the acid sites by exchanging the sites with silanol group [73,74] or alkaline/alkaline earth metals [80] to prevent coke formation. These studies reported that selectivity to benzene as well as catalytic stability increased by blocking acid sites [73,74,80,81]. In addition, increasing base sites could be effect for suppressing coke formation by enhancing adsorption of CO_2. In

dry reforming reaction in which methane and CO_2 are used for the feed, the catalyst which possessed more base sites had higher CO_2 conversion, leading to higher activity and stability [82-84]. To incorporate base sites, alkaline/alkaline earth metal oxides have been applied [82,85,86], and MgO was most widely used as the basic catalyst support [83,84,87].

In this study, CO_2 was co-fed in shale gas aromatization, and Mg was used as the promoter for Mo/ZSM-5 in order to enhance catalytic stability by suppressing coke formation. There is a previous study which improved catalytic activity using Mg-Mo/HZSM-5, which was synthesized by co-impregnation of Mo and Mg, for CO_2 co-feeding methane aromatization [88]. However, our study discovered that sequential impregnation of Mg after the impregnation of Mo on HZSM-5 was more effective than the co-impregnation. In short, we evaluated catalytic performance during shale gas aromatization depending on CO_2 concentration. Then, we investigated the effect of Mg addition on Mo/HZSM-5 focusing on acid and base properties of catalysts.

3.2. Experimental

3.2.1. Catalyst preparation

The catalyst support, HZSM-5, was obtained by the calcination of commercial ZSM-5 (Si/Al_2=23, Alfa Aesar) at 500 ˚C for 4 h. Mo was impregnated on the HZSM-5 with an aqueous solution of

$(NH_4)_6Mo_7O_{24}\cdot 4H_2O$ (Sigma Aldrich) as a metal precursor, with the intended Mo loading of 10 wt.%. The impregnated sample was dried at 105 ˚C overnight and calcined in a muffle at 500 ˚C for 6 h. The synthesized catalyst was nominated as Mo/ZSM-5.

Impregnation of Mg was carried out by two different methods using $Mg(NO_3)_2\cdot 6H_2O$ (Alfa Aesar) as a metal precursor. First, Mo and Mg was co-impregnated on HZSM-5 with the intended loading of 10 wt.% and 1 wt.% for Mo and Mg, respectively. Then, the co-impregnated sample was dried and calcined as above. The calcined catalyst was designated as Mg-Mo/ZSM-5(co). On the other hand, Mg was impregnated on calcined Mo/ZSM-5 using an aqueous solution of $Mg(NO_3)_2\cdot 6H_2O$, with the same loading with Mg-Mo/ZSM-5(co). After sequential impregnation, the catalyst undergoes same drying and calcination procedure. This sequentially impregnated catalyst was designated as Mg/Mo/ZSM-5(seq).

3.2.2. Reaction and regeneration procedure

Prior to the reaction, 0.2 g of the catalyst was pretreated in-situ in a fixed-bed quartz reactor to convert MoOx to the active phase, MoCx. Pretreatment gas composed of 45 vol.% CH_4, 5 vol.% He, and 50 vol.% Ar passed through the reactor with total flow rate of 20 ml/min. The reactor was heated to 400 ˚C with a ramping rate of 20 ˚C/min then heated to 650 ˚C with a ramping rate of 10 ˚C/min and maintained at 650 ˚C for 35 min.

After the pretreatment, the reactor was heated to 750 ℃, and the shale

gas aromatization was initiated by feeding $CH_4/C_2H_6/C_3H_8/He$ (4.25:0.5:0.25:5.6) gas mixture with flow rate of 10.6 ml/min at atmospheric pressure. In case of CO_2 co-feeding shale gas aromatization, the feed was changed to $CH_4/C_2H_6/C_3H_8/CO_2/He$ gas mixture, and the content of CO_2 varied from 5 to 10% in shale gas, fixing the total flow rate at 10.6 ml/min.

The regeneration test was conducted for CO_2 (5%) co-feeding shale gas aromatization. After 580 min of reaction, the reactor was cooled down to 550 °C and regeneration process was applied at 550 °C for 1 hour. The regeneration gas was composed of 10 vol.% O_2, 40 vol.% N_2, and 50 vol.% Ar.

The effluent gases were analyzed at 40 min of intervals by an on-line gas chromatograph (YL6500GC). Hydrocarbons were detected with a flame ionization detector, while He, H_2, CH_4, CO and CO_2 were detected with a thermal conductivity detector. To avoid the condensation of heavy hydrocarbons, outlet gas lines and sampling valve were heated to 230 ˚C. Carbon conversion, selectivity, and yield containing products were calculated based on carbon mass balance by using He as an internal standard. Also, H_2 yield was calculated based on hydrogen mass balance using the same internal standard.

3.2.3. Catalyst characterization

The metal contents of fresh catalysts were determined by inductively

coupled plasma-atomic emission spectroscopy (ICP-AES) in an OPTIMA 8300 (Perkin-Elmer).

The crystal structure of the catalysts was identified by using the powder X-ray diffraction (XRD) which was conducted on a SmartLab (Rigaku) with Cu Kα radiation. The XRD patterns were collected in a 2θ range from 5° to 50° with a step size of 0.02°.

Temperature programed reduction by H_2 (H_2–TPR) was conducted on a TCD in a BEL-CAT-II (MicrotracBEL, Corp.) instrument. Prior to analysis, 0.03 g of catalyst was heated to 400 °C for 1 h in He flow. The catalyst was then cooled down to 40 °C and heated to 1,100 °C with 5% H_2/Ar flow at a rate of 5 °C/min.

Temperature programmed desorption of NH_3 (NH_3–TPD) and CO_2 (CO_2-TPD) was conducted in a BEL-CAT BASIC (BEL Japan Inc.). After impurities on samples were removed under He flow at 300 °C for 1 h, samples were exposed to 5 % NH_3/He or 100 % CO_2 at 50 °C for 30 min for the adsorption of probe molecules. To eliminate weakly adsorbed molecules, samples were purged under He flow at 50 °C for 1 h. For the desorption of chemisorbed species, samples were heated to 650 °C under He flow at 10 °C/min, and effluent gas was detected by with a thermal conductivity detector (TCD) and a mass spectrometer (MS, Hiden Analytical).

The number of Brønsted and Lewis acid sites were quantified by Fourier

transform infrared (FT-IR) spectrometer (Nicolet 6700, Thermo Fisher Scientific) using pyridine as a probe molecule. The sample was loaded on a wafer and then purged at 400 °C for 30 min under N_2 flow. After collecting the background spectra at 150 °C, pyridine vapor was introduced to the cell at 150 °C. Then, the cell was evacuated at 150 °C for 1 h to remove weakly adsorbed pyridine molecules. The concentration of Brønsted and Lewis acid sites was calculated from the integrated areas of the bands at 1547 cm^{-1} and 1455 cm^{-1}, respectively, using the integrated molar extinction coefficients of 1.67 cm/μmol for Brønsted and 2.22 cm/μmol for Lewis acid sites [89].

X-ray photoelectron spectroscopy (XPS) analyses were performed in a K-alpha (Thermo Scientific Inc., U.K.) using monochromated Al Kα X-ray (1486.6 eV, 36W). The binding energy scale was calibrated by referring to the Si 2p at 102.8 eV as internal references.

The coke content in all spent catalyst samples was quantified using a thermogravimetric (TG) analyzer (SDT Q600, TA Instrument). Samples were heated in alumina crucibles at a rate of 5 °C/min to 700 °C in air stream to obtain the TG profile of the sample. The weight loss in the region of 375–625 °C was used to estimate the coke content.

3.3. Results and Discussion

3.3.1. Effect of CO_2 concentration and Mg addition on shale gas aromatization over Mo/ZSM-5

Conversions of methane, ethane, and propane according to CO_2 concentration are presented in Figure 3-1. For CO_2 10% co-feeding aromatization, the time scale (x axis) extended to 34 hr. Regardless of the presence of CO_2, conversion of ethane (C2) and propane (C3) were 100 % at the initial reaction. After the catalysts were completely deactivated, conversion of ethane and propane converged to 63% and 92%, respectively, owing to thermal cracking of ethane and propane [90]. This was evidenced by high selectivity towards ethylene and propylene after the deactivation (Figure 3-3). Meanwhile, methane conversion showed a negative value because methane production rate from cracking or methanation was higher than methane consumption rate. When Mg was added to Mo/ZSM-5, especially over Mg/Mo/ZSM-5(seq), conversions of ethane and propane lasted 100% for longer time while they eventually leveled off at similar values without Mg.

Yields of BTX and H_2 depending on CO_2 concentration are shown in Figure 3-2. In case of Mo/ZSM-5 during non-CO_2 aromatization, the highest BTX yield was 18.2% at 140 min then decreased to 0.9% at 380 min. The rapid deactivation of Mo/ZSM-5 originated from coke which blocked pore openings of the zeolite and hindered accessibility of reactants to the active

sites [47,91]. When 5% of CO_2 was added, the highest BTX yield decreased to 15.1% at 340 min and then to 0.9% at 660 min. When 10 % of CO_2 was co-fed with the shale gas, the yield further decreased to 10.6 %, but it dropped to 1.0 % after 21 hr of reaction. By co-feeding CO_2, BTX yield could decrease due to the oxidation of MoCx [79,92], or equilibrium shift by H_2 [77,79]. Instead of the loss of BTX yield, the catalytic stability was promoted significantly due to coke removal via Reverse Boudouard Reaction or methanation of coke via dry reforming reaction. The effect of the enhanced stability was substantial in that total amount of BTX produced during the reaction increased as concentration of CO_2 increased to 10% (Table 3-1).

Although initial conversions of hydrocarbons were similar regardless of CO_2 addition, product selectivity (Table 3-2) were varied depending on the CO_2 concentration. As CO_2 concentration increased, selectivity to BTX decreased whereas the proportion to CO selectivity increased. Considering that CO_2 was included in the feed when calculating the yield and selectivity, actual formation rate of products were compared in Figure 3-3. It could be seen that the formation rate of BTX decreased with increasing CO_2 concentration. Therefore, it was confirmed that the CO_2 addition resulted in lower BTX yield and formation rate.

Meanwhile, the addition of Mg on Mo/ZSM-5 improved activity and stability of Mo/ZSM-5, and the enhancement was more remarkable when CO_2 concentration increased (Table 3-1). Compared to Mo/ZSM-5, Mg-

Mo/ZSM-5(co) and Mg/Mo/ZSM-5(seq) increased the highest BTX yield by 0.7–1.0% (Figure 3-2). The increased yield over Mg containing catalysts was the result of enhanced selectivity to BTX, which was increased by 0.8–2.5% (Table 3-2). Especially, Mg/Mo/ZSM-5(seq) significantly enhanced stability of Mo/ZSM-5 as catalyst lifetime extended from 11 hr to 14 hr 20 min for CO_2 (5%) co-feeding, and from 21 hr to 31 hr 40 min for CO_2 (10%) co-feeding reaction. Mg-Mo/ZSM-5(co) also improved stability of Mo/ZSM-5 as the lifetime extended from 11 hr to 12 hr 20 min for CO_2 (5%) co-feeding, and from 21 hr to 26 hr 20 min for CO_2 (10%) co-feeding reaction, which was inferior to Mg/Mo/ZSM-5(seq).

Also, H_2 yield was greatly affected depending on the CO_2 concentration in the feed (Figure 3-2). For non-CO_2 reaction over Mo/ZSM-5, H_2 yield was 13.3% at the initial stage and continued to decrease. It should be noticed that the initial H_2 yield increased to 14.4% in CO_2 (5%) co-feeding and to 16.4% in CO_2 (10%) co-feeding reaction. As BTX yield decreased when CO_2 was fed, it could be predicted that H_2 production from aromatization of hydrocarbons decreased after CO_2 co-feeding. Nevertheless, total amount of H_2 increased owing to dry reforming reaction between CO_2 and hydrocarbons. However, the difference in H_2 yield depending on catalysts was insignificant despite of higher BTX yield over Mg-Mo/ZSM-5(co) and Mg/Mo/ZSM-5(seq). This might be caused by lower selectivity to $C_{10}H_8$ or H_2 consumption by coke hydrogenation [93] over Mg added catalysts.

Figure 3-4 displays CO_2 conversion and $CO_{(out)}/CO_{2(in)}$ ratio during CO_2 co-feeding aromatization. While BTX yield was above 1%, CO_2 conversion was 100% and $CO_{(out)}/CO_{2(in)}$ ratio was maintained at 2. The $CO_{(out)}/CO_{2(in)}$ ratio of 2 indicates that the total amount of CO_2 injected was converted to CO without reverse water gas shift reaction. When BTX yield decreased less than 1%, CO_2 conversion and $CO_{(out)}/CO_{2(in)}$ ratio started to decrease rapidly to 0.

To sum up, CO_2 reduced the maximum BTX yield, but it improved catalytic stability significantly, resulting in increased total amount of BTX. The addition of Mg, especially for Mg/Mo/ZSM-5(seq), further increased the stability as the concentration of CO_2 increased.

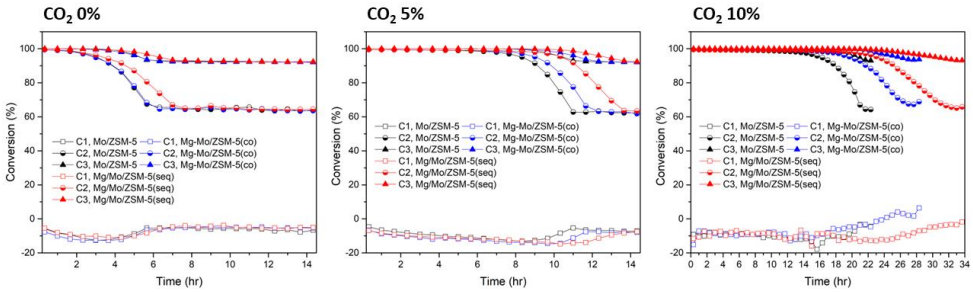

Figure 3-1. Conversion of methane, ethane and propane during catalytic dehydro-aromatization depending on CO_2 concentration.

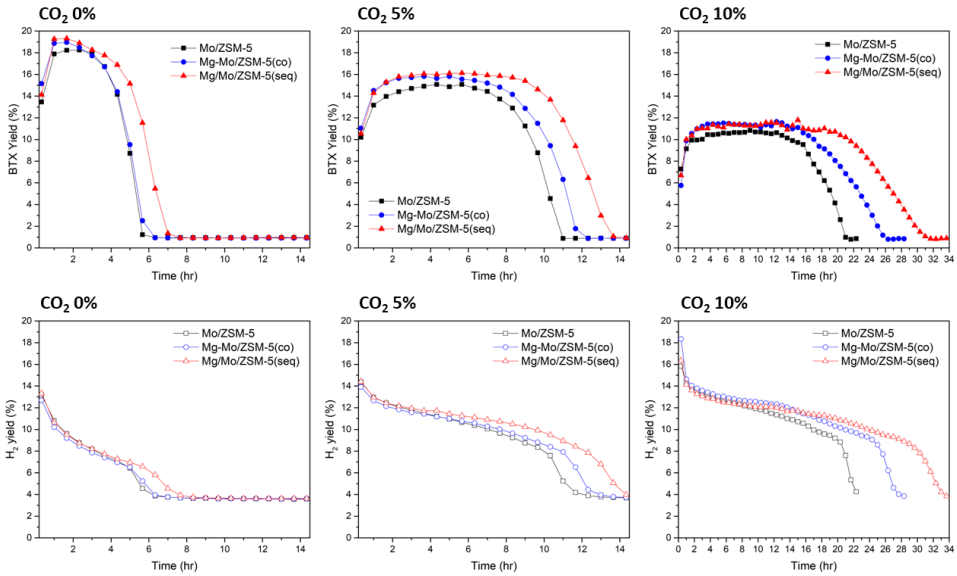

Figure 3-2. Yield of BTX and H_2 during catalytic dehydro-aromatization depending on CO_2 concentration.

Table 3-1. Deactivation time and total amount of BTX produced during the reaction.

Catalyst	Deactivation time (BTX yield ≤ 1%)			Total amount of BTX (mmol/g_{cat})		
	CO_2 0%	CO_2 5%	CO_2 10%	CO_2 0%	CO_2 5%	CO_2 10%
Mo/ZSM-5	6 hr 20 min	11 hr	21 hr	10.7	18.8	27.4
Mg-Mo/ZSM-5(co)	6 hr 20 min	12 hr 20 min	26 hr 20 min	11.1	21.5	34.7
Mg/Mo/ZSM-5(seq)	7 hr 40 min	14 hr 20 min	31 hr 40 min	13.4	25.1	41.6

Table 3-2. Product selectivity of catalysts during the reaction.

Catalysts	C_2H_4	C_3H_6	C_6H_6	C_7H_8	C_8H_{10}	$C_{10}H_8$	CO
CO_2 0% [a]							
Mo/ZSM-5	2.52	0.10	78.10	3.66	0.13	15.49	
Mg-Mo/ZSM-5(co)	2.73	0.13	78.89	4.09	0.16	14.01	
Mg/Mo/ZSM-5(seq)	2.48	0.10	80.17	4.10	0.17	12.98	
CO_2 5% [b]							
Mo/ZSM-5	1.24	0.05	50.51	2.05	0.09	11.27	34.79
Mg-Mo/ZSM-5(co)	1.41	0.05	52.31	2.23	0.10	9.62	34.28
Mg/Mo/ZSM-5(seq)	1.41	0.05	53.02	2.22	0.09	9.62	33.58
CO_2 10% [c]							
Mo/ZSM-5	1.22	0.04	33.77	1.32	0.06	8.17	55.43
Mg-Mo/ZSM-5(co)	1.18	0.04	36.37	1.47	0.07	6.34	54.52
Mg/Mo/ZSM-5(seq)	1.14	0.04	35.85	1.45	0.07	6.16	55.28

a: Relative selectivity at 100 min of reaction
b: Relative selectivity at 220 min of reaction
c: Relative selectivity at 320 min of reaction

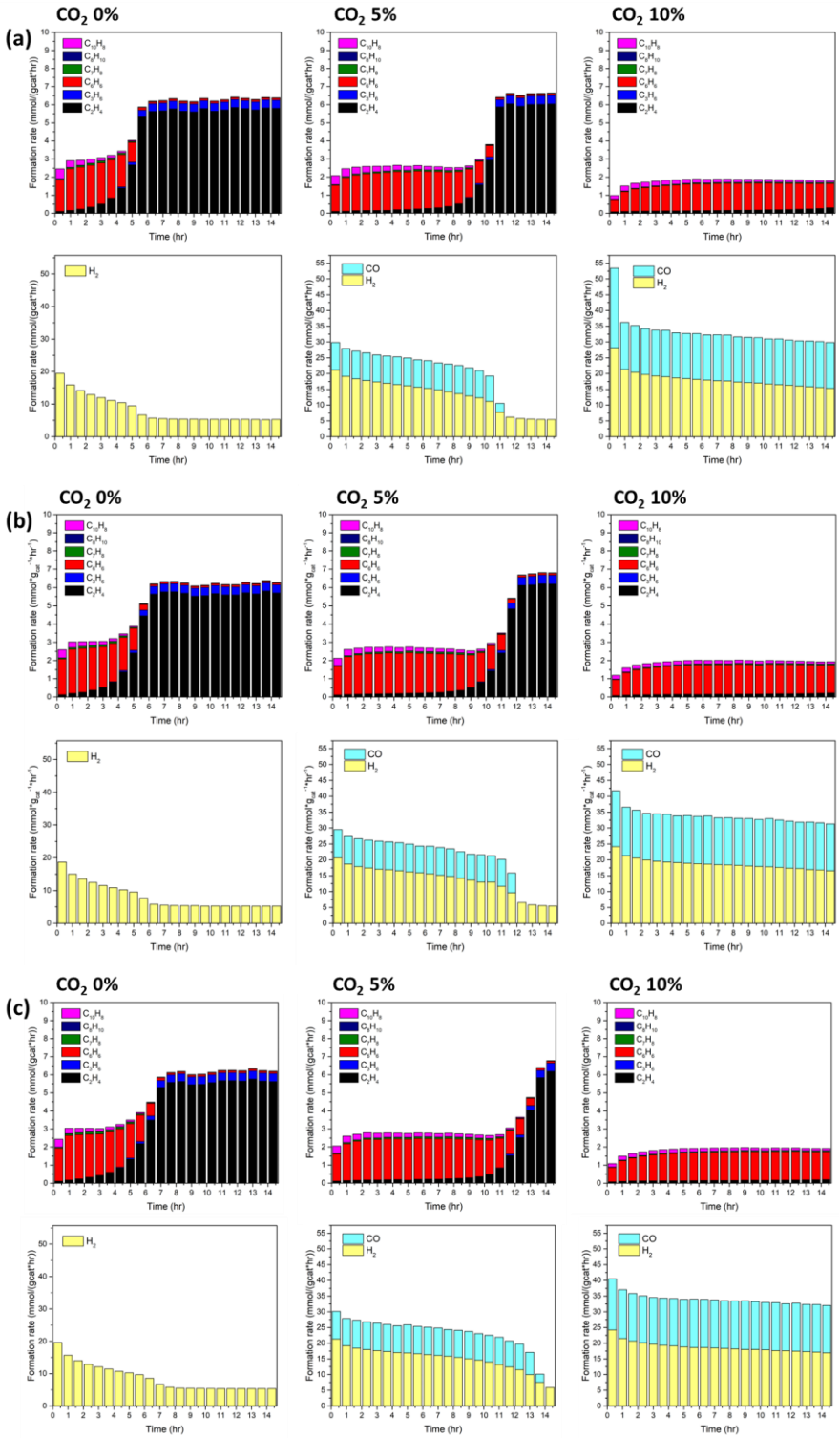

Figure 3-3. Product distributions of Mo/ZSM-5 (a), Mg-Mo/ZSM-5(co) (b), and Mg/Mo/ZSM-5(seq) (c).

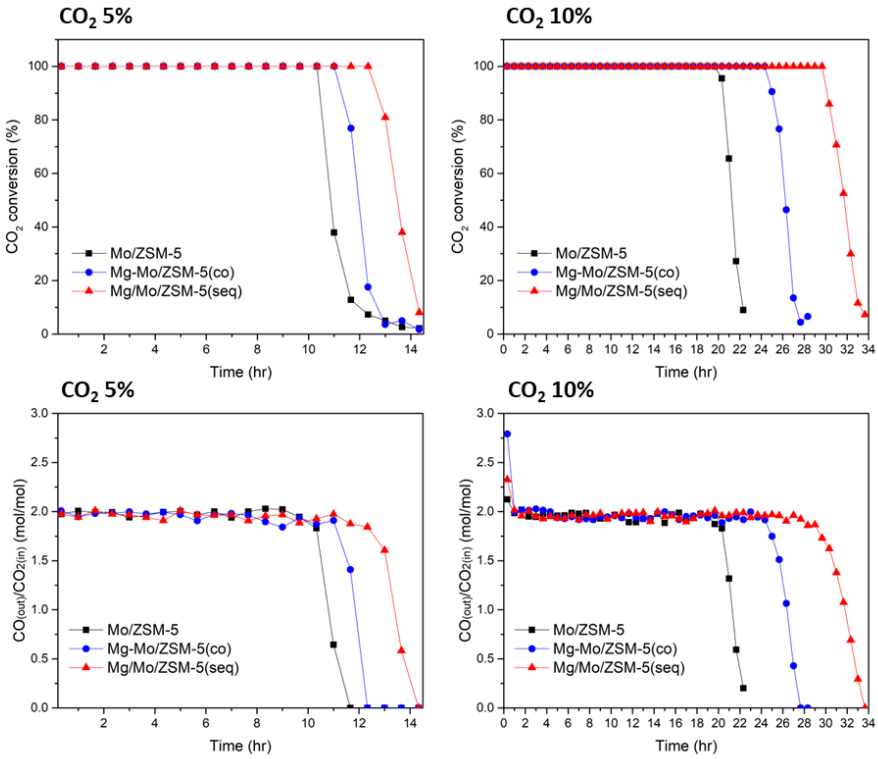

Figure 3-4. CO_2 conversion and $CO_{(out)}/CO_{2(in)}$ ratio during catalytic dehydro-aromatization depending on CO_2 concentration.

3.3.2. Identification of metal oxides in fresh catalysts

The metal contents in fresh catalysts are shown in Table 3-3. The content of Mo in Mg-Mo/ZSM-5(co) and Mg/Mo/ZSM-5(seq) was 9.4 wt.%, which was 1 wt.% lower than Mo/ZSM-5. Despite its lower content of Mo, it was found that Mg addition improved catalytic activity. Meanwhile, the content of Mg in Mg-Mo/ZSM-5(co) and Mg/Mo/ZSM-5(seq) was 0.91 wt.% and 0.99 wt.%, respectively.

In order to examine the effect of 0.08 wt.% of difference in Mg loading, catalysts with various Mg content was investigated in CO_2 5% co-feeding aromatization (Figure 3-5). The content of Mg in Mg/Mo/ZSM-5(seq) was varied to 0.5–1.5 wt.%, and 1 wt.% was found to be the optimum. Mg(0.5)/Mo/ZSM-5(seq) which had lower Mg content by 0.5 wt.% than Mg/Mo/ZSM-5(seq) was deactivated after 820 min of reaction, which had higher stability than Mg-Mo/ZSM-5(co). As Mg content in Mg-Mo/ZSM-5(co) was lower by 0.08 wt.% than Mg/Mo/ZSM-5(seq), the difference in Mg content was too small to explain the large difference in catalytic stability. Therefore, it can be concluded that the difference in the stability of Mg-Mo/ZSM-5(co) and Mg/Mo/ZSM-5(seq) resulted from the impregnation sequence rather than the slight difference in Mg content.

Figure 3-6 displays XRD patterns of fresh catalysts. Similar XRD patterns between the parent HZSM-5 and metal loaded catalysts implies that the framework of ZSM-5 was retained after the impregnation. XRD peak at 27.40^{o} refers to external MoO_3 since Mo oxide species inside the pore is too

small to be detected [94]. Intensity of external MoO_3 peak on Mg-Mo/ZSM-5(co) and Mg/Mo/ZSM-5(seq) was lower than Mo/ZSM-5, indicating that sintering of external Mo oxide was suppressed on Mg containing catalysts. This could be observed by TEM-EDS (Figure 3-7), which shows less sintering of Mo oxide on Mo/ZSM-5(co) and Mg/Mo/ZSM-5(seq). Mg related species such as MgO, $MgCO_3$ and $MgMoO_4$ were not observed in XRD spectra.

Figure 3-8 shows H_2 consumption of fresh catalysts during H_2–TPR analysis. In case of Mo/ZSM-5, reduction peaks at 476 ℃ and at 709 ℃ are attributed to the reduction of external MoO_3 to MoO_2 and and external MoO_2 to Mo metal, respectively [95]. The reduction peak at 981 ℃ is ascribed to $(Mo_2O_5)^{2+}$ anchoring with acid site of the zeolite [80,95]. In case of Mg contained catalysts, the intensity of the external MoO_3 reduction peak decreased and new peak at 631 ℃ appeared. Importantly, MoOx reduction peak at 476 ℃ and at 709 ℃ shifted most considerably over Mg/Mo/ZSM-5(seq). The new peak was not attributed to the reduction of MgO as MgO could not be reduced below 1,100 ℃ [96]. Moreover, the reduction peak of $(Mo_2O_5)^{2+}$ shifted to higher temperature around 1,100 ℃.

When Mg was added, the reduction temperature of external and internal Mo oxide species shifted owing to the interaction with non-reducible Mg species. It was reported that reduction temperature of bulk $MgMoO_4$ was 300-350 ℃ higher than bulk MoO_3 during H_2-TPR, explaining that interaction between Mg and Mo increased reduction temperature of MoO_3

[97]. The strong interaction between Mg and Mo was reported in previous studies, explaining that the interaction originated from high co-ordination strength of MgO-Mo [96]. To support the close interaction between Mg and Mo, STEM-EDS images of external particles on Mg-Mo/ZSM-5(co) and Mg/Mo/ZSM-5(seq) are shown in Figure 3-9. It can be seen that most of the region where Mo and Mg existed overlapped, indicating that MgO atoms were adjacent to MoOx atoms and affected their reducibility.

Although new metal oxide phase could not be observed through XRD, the interaction between Mo oxide and Mg oxide was discovered by H_2-TPR and STEM-EDS. The largest shift of reduction temperature over Mg/Mo/ZSM-5(seq) demonstrated that the interaction between MoOx and MgO was the most significant on Mg/Mo/ZSM-5(seq), demonstrating that the number of MgO adjacent to MoOx was the largest on Mg/Mo/ZSM-5(seq). The effect of the increased interaction between Mg and Mo will be discussed in the next section.

Table 3-3. Metal loading of catalysts obtained by ICP-AES.

Catalyst	Metal loading (wt.%)		
	Mo	Mg	Al
Mo/ZSM-5	10.4	-	2.7
Mg-Mo/ZSM-5(co)	9.4	0.91	2.9
Mg/Mo/ZSM-5(seq)	9.4	0.99	3.0

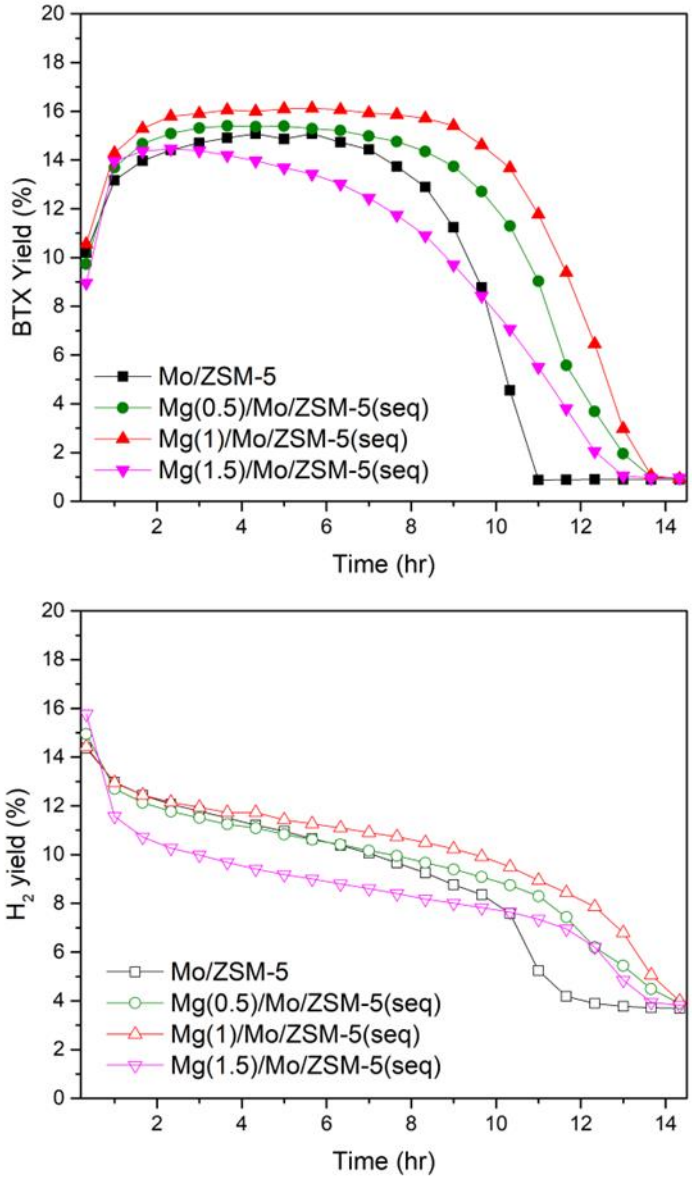

Figure 3-5. Yield of BTX and H_2 during CO_2 (5%) co-feeding shale gas aromatization in Mg/Mo/ZSM-5(seq).

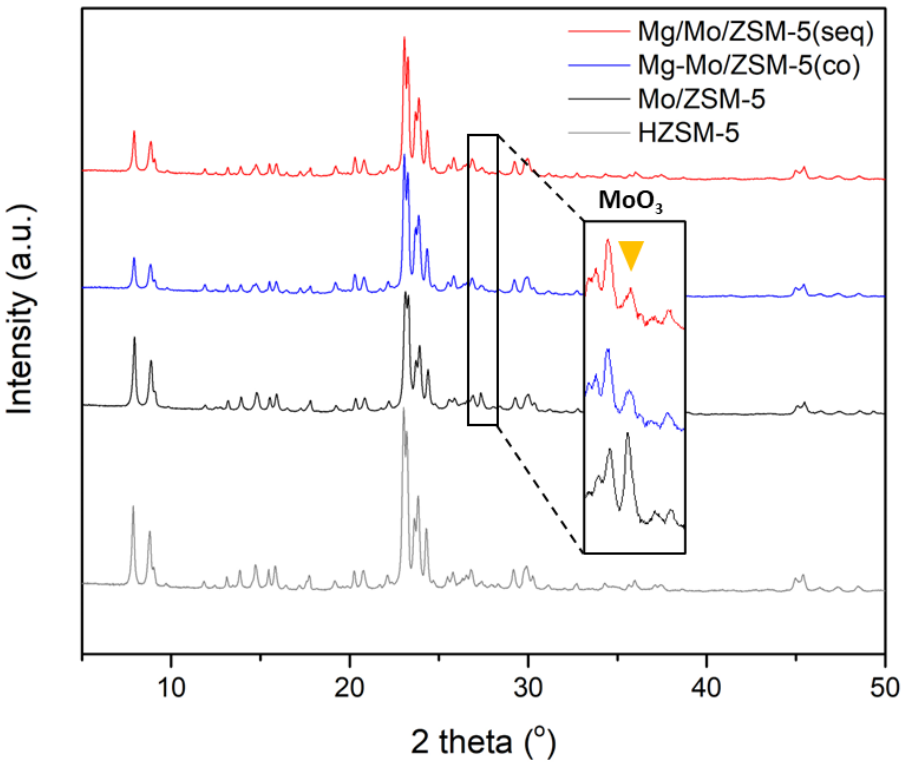

Figure 3-6. XRD spectra of fresh catalysts.

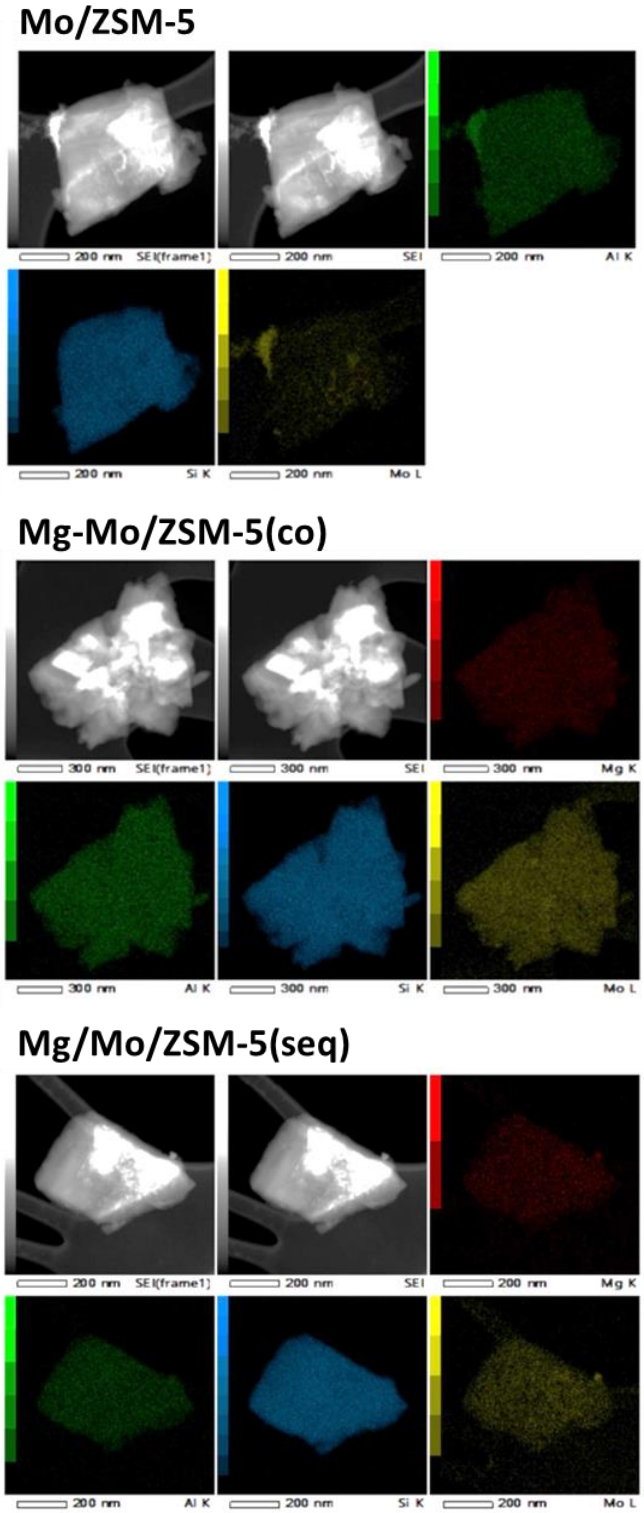

Figure 3-7. TEM-EDS images of fresh catalysts.

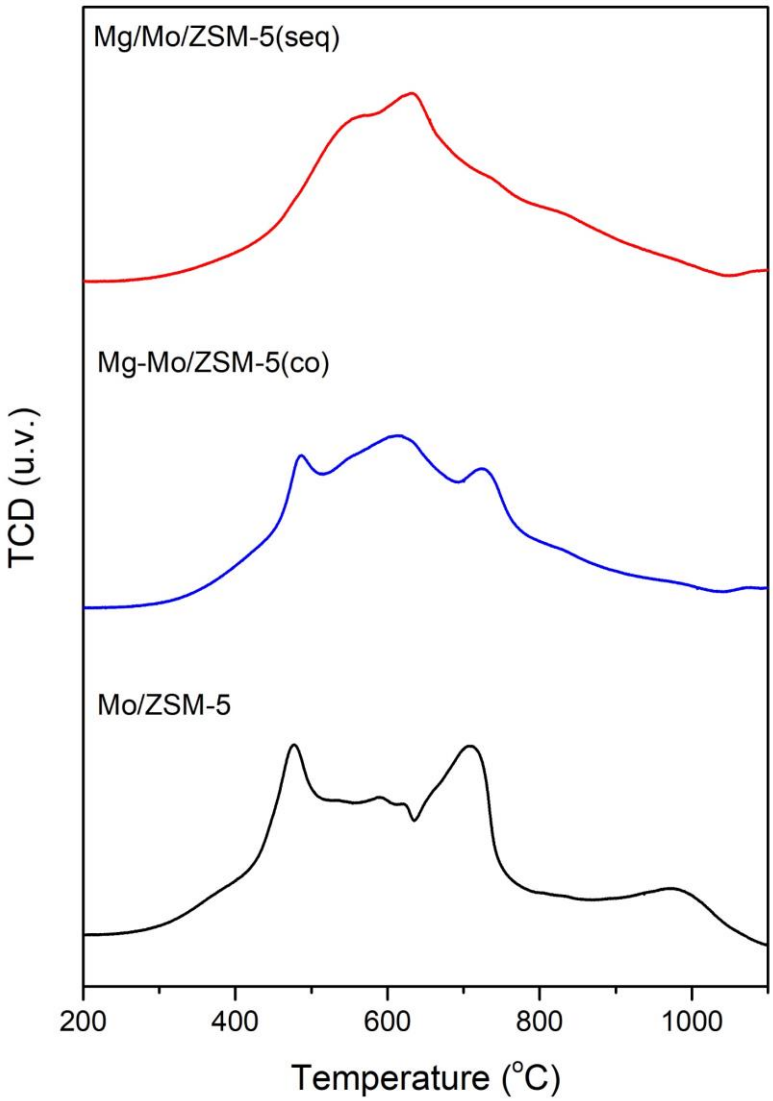

Figure 3-8. H_2-TPR of fresh catalysts.

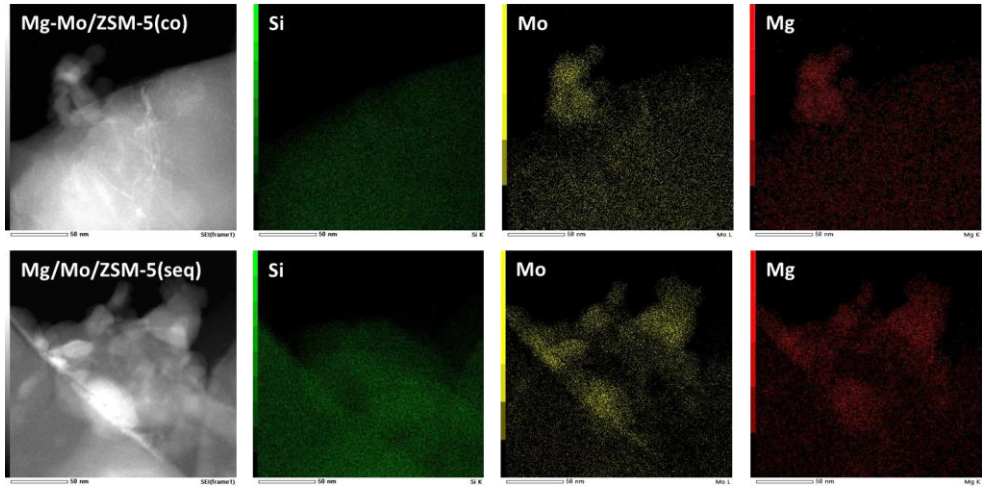

Figure 3-9. STEM-EDS images of external particles on fresh Mg-Mo/ZSM-5(co) and Mg/Mo/ZSM-5(seq).

3.3.3. Acid and base properties of fresh catalysts

It was reported that molybdenum oxide was anchored to the Brønsted acid site (BAS) of the zeolite during the calcination step [14], and magnesium oxide could be incorporated by the ion-exchange with BAS during the impregnation step [98]. Therefore, quantification of the acid sites could give evidence of the number of anchored metals. NH_3-TPD was applied for the quantification of total acid sites (Figure 3-10 (a)), and pyridine IR (Figure 3-11) was conducted to calculate the ratio of Brønsted acid site/Lewis acid site (BAS/LAS). Quantification results of acid sites are listed in Table 3-4. BAS/LAS ratio was 0.33 over Mo/ZSM-5, but it decreased to 0.26 over Mg-Mo/ZSM-5(co) and to 0.07 over Mg/Mo/ZSM-5(seq). Compared to Mo/ZSM-5 with 342 μmol/g of BAS and Mg-Mo/ZSM-5(co) with 291 μmol/g of BAS, Mg/Mo/ZSM-5(seq) had the least number of BAS of 65 μmol/g. Although it could not be distinguished whether the acid sites were removed by Mg or Mo, the change of acid distribution indicates that BAS was selectively removed after the addition of Mg, especially by sequential impregnation. The removal of BAS affected the product selectivity, as can be seen in Table 3-2; since excess oligomerization of hydrocarbons could be suppressed with the removal of BAS [74], the selectivity to BTX increased and selectivity to $C_{10}H_8$ decreased on Mg containing catalysts.

In addition, base sites were quantified by CO_2-TPD to compare the CO_2

adsorption capacity (Figure 3-10 (b)). The number of base sites over Mo/ZSM-5 was 5.3 μmol/g, while Mo/ZSM-5(co) was 7.5 μmol/g and Mg/Mo/ZSM-5(seq) was 9.7 μmol/g. If total additional base sites were derived from MgO, 19.6 % of Mg accounted for the additional base sites over Mg-Mo/ZSM-5(co), and 36.0 % over Mg/Mo/ZSM-5(seq). As MgO is known to have stronger basicity than MoCx [99], the addition of MgO provided stronger CO_2 adsorption sites on the catalysts. These base sites were efficiently increased by sequential impregnation, which had the highest density of base sites. This result could be predicted by H_2-TPR, which indicated that the largest number of MgO was adjacent to MoOx on Mg/Mo/ZSM-5(seq).

Combined analysis of NH_3 and CO_2-TPD demonstrated that MgO reduced the number of BAS and increased base sites simultaneously. Since excess free BAS site is susceptible to coke deposition due to its strong acidity, removal of the free BAS would alter coke distribution [47,73,74], which will be investigated in the section 3.5. On the other hand, since CO_2 favors to be activated on base sites [100,101], the introduction of strong base sites, MgO, would change the interaction between MoCx and CO_2. The evidence of this assumption will be suggested in the following section.

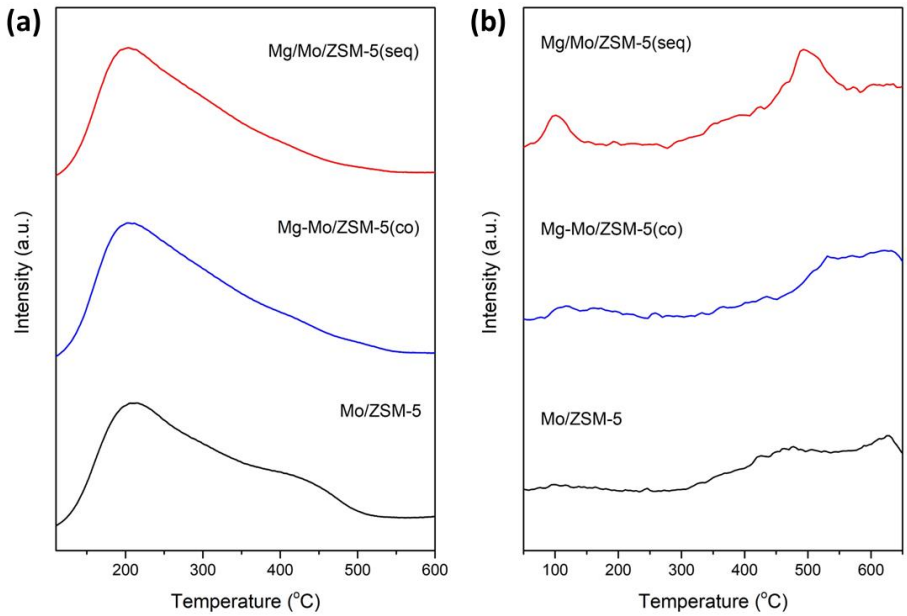

Figure 3-10. NH_3-TPD (a) and CO_2-TPD (b) results of fresh catalysts.

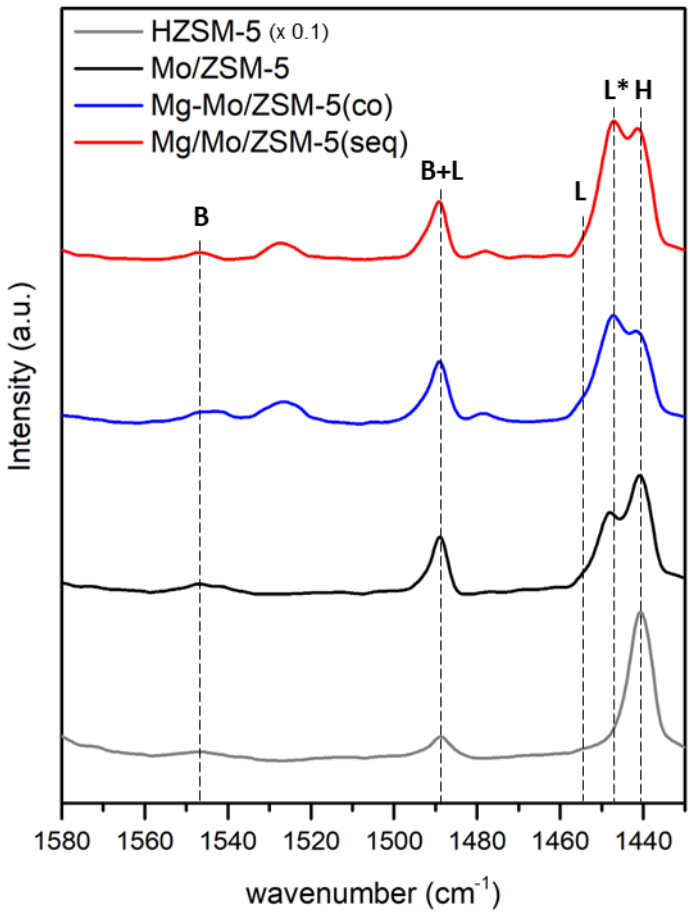

Figure 3-11. FT-IR spectra of pyridine over fresh samples. H: hydrogen bonded pyridine; L: Lewis acid bound pyridine; L*: Lewis acid related to metal sites bound pyridine; B: Brønsted acid bound pyridinium ion.

Table 3-4. Acid and base properties of fresh catalysts.

Catalysts	Brønsted acid site (μmol/g)	Lewis acid site (μmol/g)	Brønsted/Lewis acid site ratio (B/L)	NH_3 adsorbed (μmol/g)	CO_2 adsorbed (μmol/g)
Mo/ZSM-5	342	1,040	0.33	1,382	5.3
Mg-Mo/ZSM-5(co)	291	1,104	0.26	1,395	7.5
Mg/Mo/ZSM-5(seq)	65	972	0.07	1,037	9.7

3.3.4. Oxidation state of surface metal species during the reaction

The oxidation state of surface magnesium and molybdenum species of 1 hr reacted catalysts was examined by XPS. Catalysts were collected after 1 hr of non-CO_2 and CO_2 (5%) co-feeding shale gas aromatization. Firstly, Mg 1s XP spectra (Figure 3-12) during non-CO_2 reaction showed a weak peak at 1303.6-1304.3 eV, which is assigned to MgO [102]. No other peaks belonging to metallic Mg or other state of Mg were observed, informing that MgO was not reduced during the reaction. The weak intensity of the peak is probably due to the coke formation on MgO. In comparison with non-CO_2 reaction catalysts, the intensity of MgO peak at 1304.5 eV increased on CO_2 (5%) co-feeding catalysts, which indicates that the presence of CO_2 prevented coke formation on MgO, and MgO acted as the CO_2 adsorption site.

In the case of molybdenum (Figure 3-13), XP spectra was divided to six peaks, which was consisted of three sets of molybdenum species with doublet splitting peaks of Mo $3d_{5/2}$ and Mo $3d_{3/2}$. Mo $3d_{5/2}$ peak at binding energy of 232.0–232.1 eV was Mo(VI), which was originated from MoO_3 [103]. The peak at binding energy of 228.8–229.0 eV was Mo(II), and the peak at binding energy of 227.6–227.8 eV was Mo(δ), both of which were assigned to MoCx. As the charge of MoCx varies from 0 to +0.3, the Mo3d peak has been deconvoluted mostly into Mo^0 adjusting the peak with Mo^{2+} [104].

Binding energy and proportion of area of each molybdenum species are listed in Table 3-5. Interestingly, Mo(VI) was observed in all catalysts including the catalysts after non-CO_2 reaction. Mo(VI) in catalysts generated during non-CO_2 reaction might be attributed to the exposure to the air during passivation step [104,105]. After CO_2 (5%) was co-fed, the proportion of Mo(VI) increased in all catalysts because of the oxidation of MoCx by CO_2 during the reaction [79,92]. Regardless of CO_2 addition, the proportion of Mo(VI) was the largest on Mo/ZSM-5 and reduced over Mg-Mo/ZSM-5(co) and Mg/Mo/ZSM-5(seq). In the case of non-CO_2 reaction, if Mo(VI) is the result of the air exposure, the strong interaction between Mg and Mo might have prevented MoCx from oxidation, leading to lower Mo(VI) proportion. On the other hand, in case of CO_2 (5%) reaction, Mo(VI) was the result of not only MoCx oxidation after the air exposure, but also the oxidation by CO_2 during the reaction. This indicates that the oxidation of MoCx was suppressed during the reaction when Mg was added on Mo/ZSM-5. According to the previous CO_2-TPD result, Mg containing catalysts had more base sites than Mo/ZSM-5, which was induced by MgO. The reaction between CO_2 and MoCx might be suppressed due to the strong basicity of MgO. Since MoCx is the active phase for aromatization, the recovery of this phase results in higher activity. Also, in case of Mg contained catalysts, there should be an alternative route of CO_2 consumption instead of the MoCx oxidation because CO_2 conversion and $CO_{(out)}/CO_{2(in)}$ ratio were the same for all catalysts before the deactivation (Figure 3). To

examine whether Mg facilitated the reaction between CO_2 and coke, analysis on coke was conducted in the next section.

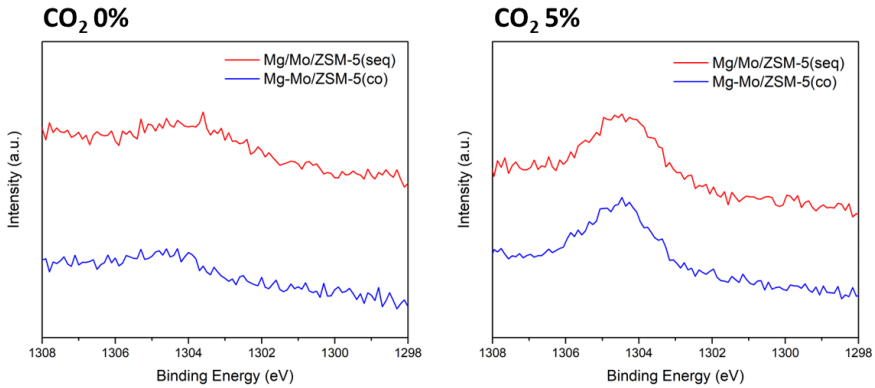

Figure 3-12. Mg 1s XP spectra of 1 hr reacted catalysts depending on CO_2 concentration.

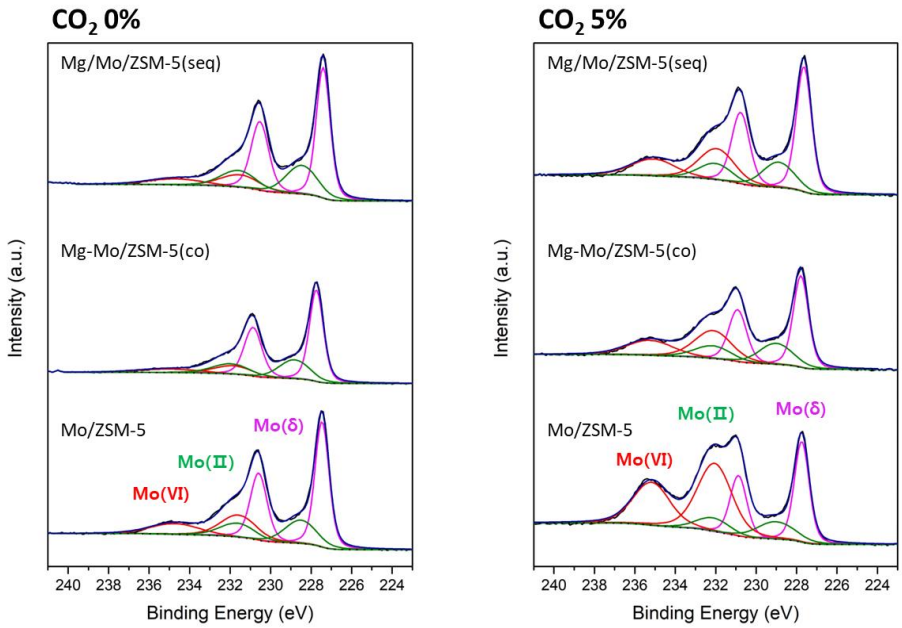

Figure 3-13. Mo 3d XP spectra of 1 hr reacted catalysts depending on CO_2 concentration.

Table 3-5. Deconvolution results of Mo 3d XPS spectra of catalysts after 1 hr of reaction.

Catalysts	Binding Energy (eV)			Area (%)		
	Mo(VI)	Mo(II)	Mo(δ)	Mo(VI)	Mo(II)	Mo(δ)
CO_2 0 %						
Mo/ZSM-5	231.6	228.5	227.5	14.5	13.8	32.5
Mg-Mo/ZSM-5(co)	231.8	228.8	227.7	8.9	15.8	35.4
Mg/Mo/ZSM-5(seq)	231.5	228.5	227.4	9.3	16.7	34.1
CO_2 5 %						
Mo/ZSM-5	232.1	228.8	227.7	31.2	9.0	19.8
Mg-Mo/ZSM-5(co)	232.1	229.0	227.8	19.9	13.5	26.6
Mg/Mo/ZSM-5(seq)	232.0	228.9	227.6	17.4	12.7	29.9

3.3.5. Coke distribution of catalysts after the reaction

The coke distribution of post-reaction catalysts was investigated by TGA. First, the amount of coke was divided by the amount of BTX produced during the reaction, and calculated results are presented in Table 5. After the addition of CO_2 (5%), the amount of coke per produced BTX decreased due to the oxidation by CO_2 or hydrogenation by H_2. In addition, the relative amount of coke decreased over Mg-Mo/ZSM-5(co) and Mg/Mo/ZSM-5(seq). Notably, in CO_2 (5%) co-feeding reaction, the amount of coke was the lowest over Mg/Mo/ZSM-5(seq). Suppression of coke by co-feeding CO_2 and Mg addition explains their improved catalytic stability.

Figure 3-14 displays DTG graph of catalysts which were classified into six peaks according to oxidation temperature, and peaks were designated as alphabet in succession from the lowest oxidation temperature. The amount of coke was quantified by integrating the peak area, of which result was shown in Table 3-6. Reactive coke, or coke located at the external surface or adjacent to MoCx was reported to be oxidized at low temperature, which is called “soft coke”. Meanwhile, inactive coke, or coke located in the internal pore or acid site was known to be oxidized at higher temperature, which is notated as “hard coke” [57,106,107]. By co-feeding CO_2, the oxidation temperature of coke decreased approximately by 50 ℃. When CO_2 was contained in the reactant, dry reforming reaction of CO_2 and hydrocarbons could be induced, yielding CO and H_2. It was reported that when H_2 was co-fed with the reactant, coke was hydrogenated by H_2, becoming surface

graphite-like coke which was oxidized at low temperature [108]. Therefore, yielding more H_2 resulted in the production of the soft coke when CO_2 was introduced.

Furthermore, the addition of Mg affected the distribution of coke. After shale gas aromatization without CO_2, the coke at the lowest temperature range, 497-516 ℃, increased on Mg contained catalysts, especially on Mg/Mo/ZSM-5(seq). This implies that production of more reactive coke was facilitated on Mg/Mo/ZSM-5(seq). Same tendency was observed on catalysts after CO_2 co-feeding aromatization; the coke at the lowest temperature range, 444-467 ℃, increased most significantly on Mg/Mo/ZSM-5(seq). Also, after CO_2 co-feeding aromatization, the oxidation temperature of the coke decreased to the greatest extent on Mg/Mo/ZSM-5(seq). In the previous section, largest proportion of MoCx was observed on Mg/Mo/ZSM-5(seq) by XPS. Therefore, higher amount of soft coke in Mg/Mo/ZSM-5(seq) might be originated from increased production of reactive coke species on MoCx. On the other hand, lower amount of hard coke in Mg/Mo/ZSM-5(seq) might be attributed to reduced amount of Brønsted acid site, which facilitates the formation of aromatic type of coke inside microchannel of the zeolite [57].

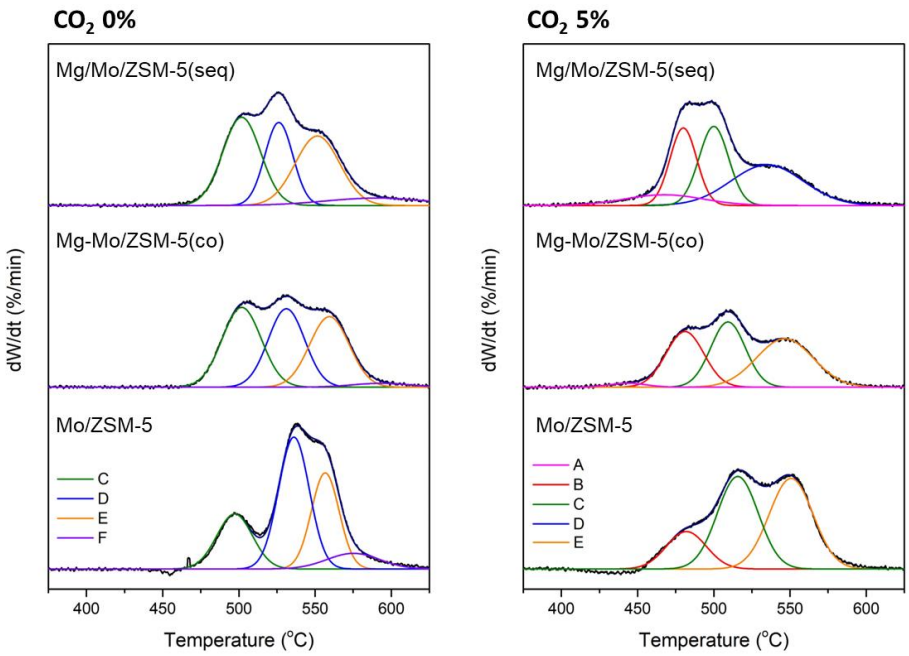

Figure 3-14. DTG graph of post-reaction catalysts depending on CO_2 concentration.

Table 3-6. Distribution of coke of post-reaction catalysts

Catalysts	Amount of coke per produced BTX (Coke g/BTX mmol)	Amount of coke (wt.%) depending on peak temperature (℃)					
		A	B	C	D	E	F
		444–467	480–482	497–516	526–536	547–559	575–593
CO_2 0 %							
Mo/ZSM-5	1.29	-	-	2.86	5.90	3.87	1.20
Mg-Mo/ZSM-5(co)	1.09	-	-	4.21	3.86	3.75	0.29
Mg/Mo/ZSM-5(seq)	1.09	-	-	5.14	3.56	4.74	1.16
CO_2 5 %							
Mo/ZSM-5	0.64	-	1.94	4.90	-	5.13	-
Mg-Mo/ZSM-5(co)	0.50	0.21	3.10	3.34	-	4.05	-
Mg/Mo/ZSM-5(seq)	0.46	1.17	2.92	3.30	4.11	-	-

3.3.6. Regeneration test on post-reaction catalysts

Since the coke distribution was changed due to the addition of Mg, the regeneration efficiency of the catalyst would also be different. As soft coke is more vulnerable to oxidation than hard coke, the post-reaction catalysts which have more proportion of the soft coke would have higher regeneration efficiency. In this respect, the regeneration test was performed over Mo/ZSM-5 and Mg/Mo/ZSM-5(seq) for CO_2 (5%) co-feeding aromatization (Figure 3-15). The catalysts were exposed to 580 min of reaction then regenerated in an oxidative atmosphere, which was repeated four times. The regeneration temperature was set to 550 ℃, at which most of the coke could be oxidized (Figure 3-14).

As reaction-regeneration cycles were repeated, Mg/Mo/ZSM-5(seq) not only promoted BTX yield, but also enhanced stability compared to Mo/ZSM-5. At the first aromatization reaction, the highest BTX yield of Mg/Mo/ZSM-5(seq) and Mo/ZSM-5 were 15.0 % and 13.9 %, respectively. The maximum BTX yield increased after the first regeneration due to re-dispersion of molybdenum oxide [61]. After the 4th regeneration, the maximum yield of Mg/Mo/ZSM-5(seq) continued to exceed over 15.0 %. However, the yield was not fully recovered over Mo/ZSM-5 yielding 13.5 % of BTX after the 4th regeneration. Furthermore, after 59 hr of reaction, BTX yield over Mg/Mo/ZSM-5(seq) was 7.0 %, but Mo/ZSM-5 was totally deactivated. Higher regeneration efficiency of Mg/Mo/ZSM-5(seq) resulted

from the formation of easily removable soft coke instead of the hard coke. However, the stability of Mg/Mo/ZSM-5(seq) was not fully recovered after the regeneration probably due to irreversible damage on zeolite framework by $Al_2(MoO_4)_3$ formation [109].

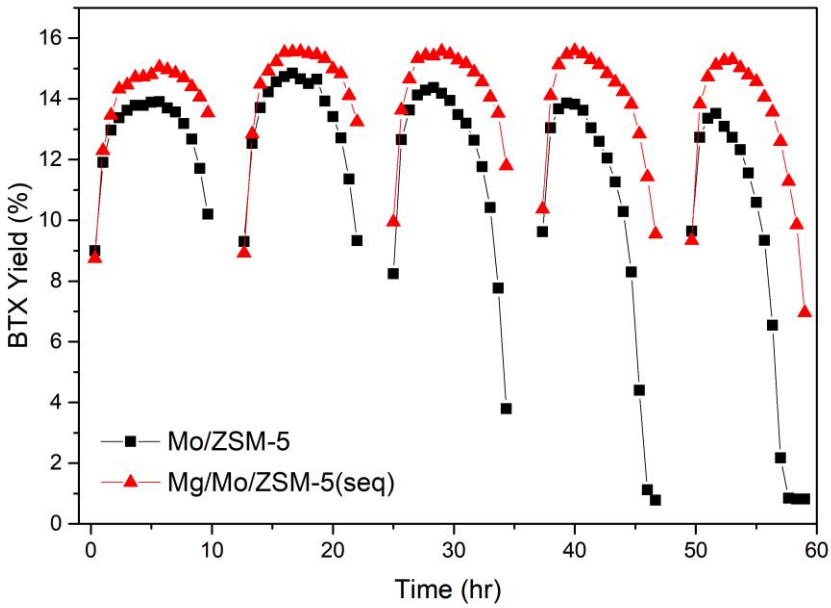

Figure 3-15. Catalytic performance of catalysts during reaction-regeneration cycles.

Chapter 4. Summary and Conclusions

In the first study, NiO particles of various sizes (4, 22, 36, 45, and 101 nm) were physically mixed with Mo/HZSM-5, resulting in different promotional effects on MDA. When the particle size of NiO was smaller than 22 nm, $NiMoO_4$ formation was facilitated by the interaction between NiO and external MoO_3. The $NiMoO_4$ formation inhibited the reduction of NiO and MoOx, resulting in the severe agglomeration and low dispersion of MoCx, which is the active phase for benzene production. The low MoCx dispersion on NiO(4nm)-Mo/HZSM-5 led to a decreased methane conversion and low BTX yield.

In the case of NiO particles larger than 36 nm, separate NiO species that did not form $NiMoO_4$ were reduced at low temperatures to form metallic Ni, decreasing the MoOx reduction temperature. The reduction of MoOx at lower temperatures restricted the agglomeration of MoOx, enhancing the MoCx dispersion. In addition, Ni facilitated the formation of CNT-type coke, enhancing catalytic stability. This explains the superior activity and stability of NiO-Mo/HZSM-5 with NiO particles larger than 36 nm compared with the activity of the other samples. In particular, NiO(36nm)-Mo/HZSM-5 exhibited the highest activity because the reduction temperatures of NiO and MoOx were the lowest.

In the second study, catalytic performances of Mg-Mo/ZSM-5(co) and Mg/Mo/ZSM-5(seq) were compared with Mo/ZSM-5. In non-CO_2 shale gas

aromatization, Mg/Mo/ZSM-5(seq) showed the highest BTX yield and the longest lifetime, which is attributed to the least number of Brønsted acid sites over Mg/Mo/ZSM-5(seq). Using Mg/Mo/ZSM-5(seq), BTX could be produced with higher selectivity instead of the accumulation to coke on the acid site. When CO_2 was added into the feed, additional effect of Mg was derived from its bascity; the largest number of base site of Mg/Mo/ZSM-5(seq) prevented oxidation of MoCx by inducing the Reverse Boudouard reaction or dry reforming reaction on the additional base site. As a result, Mg/Mo/ZSM-5(seq) improved catalytic stability most significantly and the improvement was amplified as the concentration of CO_2 increased. Also, as the production of hard coke was suppressed on Mg/Mo/ZSM-5(seq), coke was efficiently removed during the regeneration cycle, extending the lifetime of the catalyst.

Bibliography

[1] E.A. Uslamin, H. Saito, N. Kosinov, E. Pidko, Y. Sekine and E.J. Hensen, Catal. Sci. Technol. 10 (2020) 2774-2785.

[2] S.N. Malik and O.R. Sukhera, Renew. Sust. Energ. Rev. 16 (2012) 1282-1290.

[3] N. Kosinov and E.J. Hensen, Adv. Mater. 32 (2020) 2002565.

[4] J.J. Spivey and G. Hutchings, Chem. Soc. Rev. 43 (2014) 792-803.

[5] S. Yao, L. Gu, C. Sun, J. Li and W. Shen, Industrial & Engineering Chemistry Research 48 (2009) 713-718.

[6] M.Y. Gim, C. Song, Y.H. Lim, K.-Y. Lee and D.H. Kim, Catal. Sci. Technol. 9 (2019) 6285-6296.

[7] B.J. Lee, Y.G. Hur, D.H. Kim, S.H. Lee and K.-Y. Lee, Fuel 253 (2019) 449-459.

[8] C. Song, M.Y. Gim, Y.H. Lim and D.H. Kim, Fuel 251 (2019) 404-412.

[9] O.A. Anunziata, G.A. Eimer and L.B. Pierella, Applied Catalysis A: General 190 (2000) 169-176.

[10] H.M. Lee, B.J. Lee, S.Y. Kim, D.H. Kim, G.-H. Han and K.-Y. Lee, Fuel 325 (2022) 124939.

[11] W. Jung, S. Lee, H. Kim, K. Nam, H.W. Ryu, Y.H. Lim, K.-S. Ha, W.-J. Kim, D.H. Kim and J. Lee, ACS Sustainable Chemistry & Engineering 10 (2022) 5998-6011.

[12] W. Jung, S. Lee, H. Kim, K. Nam, H.W. Ryu, Y.H. Lim, K.-S. Ha, W.-J. Kim, D.H. Kim and J. Lee, Chemical Engineering Journal 450 (2022) 137992.

[13] K. Sun, D.M. Ginosar, T. He, Y. Zhang, M. Fan and R. Chen, Ind. Eng. Chem. Res. 57 (2018) 1768-1789.

[14] J. Gao, Y. Zheng, J.-M. Jehng, Y. Tang, I.E. Wachs and S.G. Podkolzin, Science 348 (2015) 686-690.

[15] U. Menon, M. Rahman and S.J. Khatib, Appl. Catal. A: Gen. (2020) 117870.

[16] S.V. Konnov, F. Dubray, E.B. Clatworthy, C. Kouvatas, J.p. Gilson, J.p. Dath, D. Minoux, C. Aquino, V. Valtchev and S. Moldovan, Angew. Chem. Int. Ed. 59 (2020) 19553-19560.

[17] P. Tan, Catal. Commun. 103 (2018) 101-104.

[18] P. Tan, Applied Catalysis A: General 580 (2019) 111-120.

[19] K. Velebná, M. Horňáček, V. Jorík, P. Hudec, M. Čaplovičová and L.u. Čaplovič, Micropor. Mesopor. Mater. 212 (2015) 146-155.

[20] T.H. Lim, K. Nam, I.K. Song, K.-Y. Lee and D.H. Kim, Appl. Catal. A: Gen. 552 (2018) 11-20.

[21] A. Martínez, E. Peris, M. Derewinski and A. Burkat-Dulak, Catal. Today 169 (2011) 75-84.

[22] A. Martínez, E. Peris and G. Sastre, Catal. Today 107 (2005) 676-684.
[23] S. Burns, J. Hargreaves, P. Pal, K. Parida and S. Parija, Catal. Today 114 (2006) 383-387.
[24] V. Fila, M. Bernauer, B. Bernauer and Z. Sobalik, Catal. Today 256 (2015) 269-275.
[25] A. Sridhar, M. Rahman, A. Infantes-Molina, B.J. Wylie, C.G. Borcik and S.J. Khatib, Applied Catalysis A: General 589 (2020) 117247.
[26] Y. Xu, J. Wang, Y. Suzuki and Z.-G. Zhang, Appl. Catal. A: Gen. 409 (2011) 181-193.
[27] Y. Xu, J. Wang, Y. Suzuki and Z.-G. Zhang, Catal. Today 185 (2012) 41-46.
[28] M. Rahman, A. Infantes-Molina, A. Boubnov, S.R. Bare, E. Stavitski, A. Sridhar and S.J. Khatib, J. Catal. 375 (2019) 314-328.
[29] K. Nam, H.W. Ryu, M.Y. Gim and D.H. Kim, Appl. Catal. B: Environ. 296 (2021) 120377.
[30] J.W. Han, J.S. Park, M.S. Choi and H. Lee, Appl. Catal. B: Environ. 203 (2017) 625-632.
[31] Y. Wang, H. Wang, A.H. Dam, L. Xiao, Y. Qi, J. Niu, J. Yang, Y.-A. Zhu, A. Holmen and D. Chen, Catal. Today 355 (2020) 139-147.
[32] H.A. Aleksandrov, N. Pegios, R. Palkovits, K. Simeonov and G.N. Vayssilov, Catal. Sci. Technol. 7 (2017) 3339-3347.
[33] J.-H. Kim, D.J. Suh, T.-J. Park and K.-L. Kim, Appl. Catal. A: Gen. 197 (2000) 191-200.
[34] S. Tang, L. Ji, J. Lin, H. Zeng, K. Tan and K. Li, J. Catal. 194 (2000) 424-430.
[35] W.-J. Jang, J.-O. Shim, H.-M. Kim, S.-Y. Yoo and H.-S. Roh, Catal. Today 324 (2019) 15-26.
[36] X. Fuku, N. Matinise, M. Masikini, K. Kasinathan and M. Maaza, Mater. Res. Bull. 97 (2018) 457-465.
[37] Y. Wang, L. Xiao, Y. Qi, J. Yang, Y.-A. Zhu and D. Chen, J. Phys. Chem. C . 124 (2020) 2501-2512.
[38] V. Abdelsayed, D. Shekhawat and M.W. Smith, Fuel 139 (2015) 401-410.
[39] Á. López-Martín, A. Caballero and G. Colón, Applied Catalysis B: Environmental 312 (2022) 121382.
[40] T.H. Lim, K. Nam, I.K. Song, K.-Y. Lee and D.H. Kim, Applied Catalysis A: General 552 (2018) 11-20.
[41] A.K. Aboul-Gheit, M.S. El-Masry and A.E. Awadallah, Fuel Processing Technology 102 (2012) 24-29.
[42] M. Ermakova, D.Y. Ermakov, L. Plyasova and G. Kuvshinov, Catal. Lett. 62 (1999) 93-97.
[43] L. Zhou, Y. Guo and K. Hideo, AlChE J. 60 (2014) 2907-2917.
[44] Q. Jeangros, T.W. Hansen, J.B. Wagner, C.D. Damsgaard, R.E. Dunin-Borkowski, C. Hebert and A. Hessler-Wyser, Journal of

Materials Science 48 (2013) 2893-2907.
[45] I. Alstrup, J. Catal. 109 (1988) 241-251.
[46] J.I. Villacampa, C. Royo, E. Romeo, J.A. Montoya, P. Del Angel and A. Monzon, Appl. Catal. A: Gen. 252 (2003) 363-383.
[47] C.H. Tempelman and E.J. Hensen, Appl. Catal. B: Environ. 176 (2015) 731-739.
[48] J.-S. Choi, G. Bugli and G. Djéga-Mariadassou, J. Catal. 193 (2000) 238-247.
[49] H. Liu, X. Bao and Y. Xu, J. Catal. 239 (2006) 441-450.
[50] D. Wang, J.H. Lunsford and M.P. Rosynek, J. Catal. 169 (1997) 347-358.
[51] A. Adam, M.H. Suliman, M. Awwad, M.N. Siddiqui, Z.H. Yamani and M. Qamar, Int. J. Hydrog. Energy 44 (2019) 11797-11807.
[52] L. Chen, L. Lin, Z. Xu, X. Li and T. Zhang, J. Catal. 157 (1995) 190-200.
[53] C. Shi, S. Zhang, X. Li, A. Zhang, M. Shi, Y. Zhu, J. Qiu and C. Au, Catal. Today 233 (2014) 46-52.
[54] A. Zhang, A. Zhu, B. Chen, S. Zhang, C. Au and C. Shi, Catal. Commun. 12 (2011) 803-807.
[55] L. Zhang, Y. Yang, Z. Yao, S. Yan and X. Kang, Catal. Sci. Technol. 11 (2021) 479-483.
[56] Y. Song, Y. Xu, Y. Suzuki, H. Nakagome, X. Ma and Z.-G. Zhang, J. Catal. 330 (2015) 261-272.
[57] Y. Song, Y. Xu, Y. Suzuki, H. Nakagome and Z.-G. Zhang, Appl. Catal. A: Gen. 482 (2014) 387-396.
[58] Y. Li, X. Zhang, X. Tao, J. Xu, W. Huang, J. Luo, Z. Luo, T. Li, F. Liu and Y. Bao, Carbon 43 (2005) 295-301.
[59] L.-P. Zhou, K. Ohta, K. Kuroda, N. Lei, K. Matsuishi, L. Gao, T. Matsumoto and J. Nakamura, The Journal of Physical Chemistry B 109 (2005) 4439-4447.
[60] H.U. Modekwe, M.A. Mamo, K. Moothi and M.O. Daramola, Catalysts 11 (2021) 692.
[61] G. Sanapur, A. Kumar, A. Mondal, S. Sreeramagiri, R. Dongara and G. Ramaswamy, J. Anal. Appl. Pyrolysis 138 (2019) 22-28.
[62] A.C. Ferrari, Solid State Commun. 143 (2007) 47-57.
[63] A.C. Ferrari and J. Robertson, Phys. Rev. B 61 (2000) 14095.
[64] B. Liu, L. Jiang, H. Sun and C. Au, Appl. Surf. Sci. 253 (2007) 5092-5100.
[65] A. Keszler, L. Nemes, S. Ahmad and X. Fang, J. Optoelectron. Adv. Mater 6 (2004) 1269-1274.
[66] P. Tan, S.L. Zhang, K.T. Yue, F. Huang, Z. Shi, X. Zhou and Z. Gu, J. Raman Spectrosc. 28 (1997) 369-372.
[67] U. Menon, M. Rahman and S.J. Khatib, Applied Catalysis A: General 608 (2020) 117870.
[68] W. Taifan and J. Baltrusaitis, Applied Catalysis B: Environmental

198 (2016) 525-547.
[69] A. Demirbas, N. Cek and S. Acar, Petroleum Science and Technology 36 (2018) 1690-1695.
[70] D.T. Allen, V.M. Torres, J. Thomas, D.W. Sullivan, M. Harrison, A. Hendler, S.C. Herndon, C.E. Kolb, M.P. Fraser and A.D. Hill, Proceedings of the National Academy of Sciences 110 (2013) 17768-17773.
[71] Y. Xiang, H. Wang, J. Cheng and J. Matsubu, Catalysis Science & Technology 8 (2018) 1500-1516.
[72] Y.H. Lim, H.W. Ryu, W. Jung, K. Nam, Y. Hwang and D.H. Kim, Fuel (2022) 126946.
[73] H. Liu, Y. Li, W. Shen, X. Bao and Y. Xu, Catalysis Today 93-95 (2004) 65-73.
[74] C.H.L. Tempelman, V.O. de Rodrigues, E.R.H. van Eck, P.C.M.M. Magusin and E.J.M. Hensen, Microporous and Mesoporous Materials 203 (2015) 259-273.
[75] A.C.C. Rodrigues and J.L.F. Monteiro, Catalysis Letters 117 (2007) 166-170.
[76] R. Ohnishi, S. Liu, Q. Dong, L. Wang and M. Ichikawa, Journal of Catalysis 182 (1999) 92-103.
[77] Z. Liu, M.A. Nutt and E. Iglesia, Catalysis letters 81 (2002) 271-279.
[78] S. Liu and Q. Dong, Chemical communications (1998) 1217-1218.
[79] H. Lacheen and E. Iglesia, Journal of Catalysis 230 (2005) 173-185.
[80] A. Martínez and E. Peris, Applied Catalysis A: General 515 (2016) 32-44.
[81] B. Xu, M. Tan, X. Wu, H. Geng, F. Song, Q. Ma, C. Luan, G. Yang and Y. Tan, Fuel 283 (2021) 118889.
[82] V. García, J.J. Fernández, W. Ruíz, F. Mondragón and A. Moreno, Catalysis Communications 11 (2009) 240-246.
[83] B. Jin, S. Li and X. Liang, Fuel 284 (2021) 119082.
[84] F. Meshkani and M. Rezaei, International journal of hydrogen energy 35 (2010) 10295-10301.
[85] Z. Alipour, M. Rezaei and F. Meshkani, Fuel 129 (2014) 197-203.
[86] N. Charisiou, A. Baklavaridis, V. Papadakis and M. Goula, Waste and biomass valorization 7 (2016) 725-736.
[87] Y. Song, E. Ozdemir, S. Ramesh, A. Adishev, S. Subramanian, A. Harale, M. Albuali, B.A. Fadhel, A. Jamal and D. Moon, Science 367 (2020) 777-781.
[88] X. Cheng, P. Yan, X. Zhang, F. Yang, C. Dai, D. Li and X.-X. Ma, Molecular Catalysis 437 (2017) 114-120.
[89] C. Emeis, Journal of Catalysis 141 (1993) 347-354.
[90] S.Y. Yu, G.J. Yu, W. Li and E. Iglesia, The Journal of Physical Chemistry B 106 (2002) 4714-4720.
[91] J. Bai, S. Liu, S. Xie, L. Xu and L. Lin, Catalysis letters 90 (2003) 123-130.

[92] P.L. Tan, K.W. Wong, C.T. Au and S.Y. Lai, Applied Catalysis A: General 253 (2003) 305-316.
[93] Y. Xu, J. Lu, J. Wang, Y. Suzuki and Z.-G. Zhang, Chemical engineering journal 168 (2011) 390-402.
[94] Y. Song, C. Sun, W. Shen and L. Lin, Applied Catalysis A: General 317 (2007) 266-274.
[95] Á. López-Martín, F. Platero, G. Colón and A. Caballero, Reaction Chemistry & Engineering 6 (2021) 1265-1276.
[96] M. Kumar, F. Aberuagba, J. Gupta, K. Rawat, L. Sharma and G.M. Dhar, Journal of Molecular Catalysis A: Chemical 213 (2004) 217-223.
[97] M.I. Fadlalla, M.D. Farahani and H.B. Friedrich, Molecular Catalysis 461 (2018) 86-96.
[98] J. Goetze and B.M. Weckhuysen, Catalysis Science & Technology 8 (2018) 1632-1644.
[99] S.K. Bej, C.A. Bennett and L.T. Thompson, Applied Catalysis A: General 250 (2003) 197-208.
[100] M. Aziz, A. Jalil, S. Wongsakulphasatch and D.-V.N. Vo, Catalysis Science & Technology 10 (2020) 35-45.
[101] N.A.K. Aramouni, J.G. Touma, B.A. Tarboush, J. Zeaiter and M.N. Ahmad, Renewable and Sustainable Energy Reviews 82 (2018) 2570-2585.
[102] J.-W. He, J. Corneille and D. Goodman, Applied surface science 72 (1993) 335-340.
[103] F. Solymosi, J. Cserényi, A. Szöke, T. Bánsági and A. Oszkó, Journal of Catalysis 165 (1997) 150-161.
[104] K. Oshikawa, M. Nagai and S. Omi, The Journal of Physical Chemistry B 105 (2001) 9124-9131.
[105] J.-Z. Zhang, M.A. Long and R.F. Howe, Catalysis today 44 (1998) 293-300.
[106] M. Rahman, A. Sridhar and S.J. Khatib, Applied Catalysis A: General 558 (2018) 67-80.
[107] D. Ma, Y. Shu, M. Cheng, Y. Xu and X. Bao, Journal of Catalysis 194 (2000) 105-114.
[108] Y. Song, Q. Zhang, Y. Xu, Y. Zhang, K. Matsuoka and Z.-G. Zhang, Appl. Catal. A: Gen. 530 (2017) 12-20.
[109] N. Kosinov, F.J. Coumans, G. Li, E. Uslamin, B. Mezari, A.S. Wijpkema, E.A. Pidko and E.J. Hensen, Journal of Catalysis 346 (2017) 125-133.

국 문 초 록

벤젠, 톨루엔 및 자일렌(BTX)은 화학 물질 및 플라스틱의 원료로, 필수불가결한 화학 물질이다. BTX는 주로 나프타로부터 생산되는데, 원유 가격의 변동성이 매우 크기 때문에 대체 연료를 찾을 필요성이 대두되고 있다. 메탄이 주성분인 천연가스는 자원량이 풍부하고 질소 및 황이 적게 포함되었어 환경 친화성인 대체 자원이다. 메탄의 무산소 탈수소 방향족화는 무산소 조건에서 메탄을 BTX 및 수소로 직접 전환시키는 반응이다. 벤젠에 대한 선택도는 60-80% 사이로 매우 높으므로, 적절한 촉매 공정을 개발한다면 그 활용도가 높다. 따라서 탈수소 방향족화의 성능을 향상시키기 위한 촉매 개발이 연구되었다.

첫 번째 연구에서는 Mo/ZSM-5의 촉진제로서 다양한 크기(4, 22, 36, 45 및 101 nm)를 갖는 NiO 입자가 메탄 탈수소 방향족화 반응에 미치는 영향을 평가하였다. NiO(36nm)는 Mo/HZSM-5의 활성을 향상시키기 위한 최적의 크기를 가지고 있음을 발견하였다. 촉매 분석 결과 NiO 및 MoOx가 가장 낮은 온도에서 환원되어 NiO(36nm)-Mo/HZSM-5의 MoCx 활성점 분산도가 가장 높았다. NiO 입자 크기가 22 nm보다 작을 때, 불활성종인 $NiMoO_4$ 형성이 선호되었고, 이는 MoCx의 응집 및 낮은 분산도를 야기하였다.

다음으로, 코크스를 억제하기 위해 반응물에 약산화제로 CO_2를 첨가하였다. CO_2 첨가는 코크스 형성을 방지할 뿐만 아니라 추가적으로 합성 가스를 생성할 수 있다는 이점이 있다. 또한, 코크스 형성을 촉진시키는 잉여 브뢴스테드 산점을 제거하거나 CO_2가 흡착될 수 있는 염기점을 늘리면 촉매가 코크스에 저항성을 가질 수 있다. 따라서 산성 또는 염기성 특성을 제어하기 위해 널리 사용되었던 Mg를 두 가지 방식으로 Mo/ZSM-5에 조촉매로 담지하였다. 공동 함침법으로 제조된 Mg-Mo/ZSM-5(co)와 Mo 담지 후 Mg을 담지하여 제조한 Mg/Mo/ZSM-5(seq)의 활성을 비교하였다. 촉매 특성 분석 결과, Mg/Mo/ZSM-5(seq)가 가장 적은 브뢴스테드 산점과 가장 많은 염기점을 가졌다는 것을 밝혔다. 이러한 산 및 염기 특성의 변화는 촉매 수율 및 안정성을 향상시켰고, CO_2 농도가 10%로 증가함에 따라 그 효과가 증폭되었다.

주요어: 천연 가스, 이산화탄소, BTX, 탈수소 방향족화, Mo/HZSM-5, NiO, Mg

학번: 2019-32752